



Chondroitin sulfate cross-linked three-dimensional tailored electrospun scaffolds for cartilage regeneration

Yujie Chen^{a,1}, Wei Xu^{b,c,d,1}, Muhammad Shafiq^{a,e,*}, Daiying Song^{b,c,d}, Xianrui Xie^a, Zhengchao Yuan^a, Mohamed EL-Newehy^f, Hany EL-Hamshary^f, Yosry Morsi^g, Yu Liu^{b,c,d,**}, Xiumei Mo^{a,***}

^a Shanghai Engineering Research Center of Nano-Biomaterials and Regenerative Medicine, State Key Laboratory for Modification of Chemical Fibers and Polymer Materials, College of Chemistry, Chemical Engineering and Biotechnology, Donghua University, Songjiang, Shanghai 201600, China

^b Research Institute of Plastic Surgery, Wei Fang Medical College, Weifang 261000, China

^c National Tissue Engineering Center of China, Minhang, Shanghai 201100, China

^d Shanghai Key Laboratory of Tissue Engineering, Department of Plastic and Reconstructive Surgery, Shanghai 9th People's Hospital, Shanghai Stem Cell Institute, Shanghai Jiao Tong University School of Medicine, Huangpu, Shanghai 200001, China

^e Department of Biotechnology, Faculty of Life Sciences (FLS), University of Central Punjab (UCP), Lahore 54000, Pakistan

^f Department of Chemistry, College of Science, King Saud University, P.O. Box 2455, Riyadh 11451, Saudi Arabia

^g Faculty of Engineering and Industrial Sciences, Swinburne University of Technology, Boroondara, VIC 3122, Australia

ARTICLE INFO

Keywords:

Electrospinning
Three-dimensional
Gas foaming
Chondroitin sulfate
Cartilage tissue engineering
Silk fibroin

ABSTRACT

Degenerated cartilage tissues remain a burgeoning issue to be tackled, while bioactive engineering products available for optimal cartilage regeneration are scarce. In the present study, two-dimensional (2DS) poly(L-lactide-co-ε-caprolactone)/silk fibroin (PLCL/SF)-based scaffolds were fabricated by conjugate electrospinning method, which were then cross-linked with chondroitin sulfate (CS) to further enhance their mechanical and biological performance. Afterwards, three-dimensional (3D) PLCL/SF scaffolds (3DS) and CS-crosslinked 3D scaffolds (3DCSS) with tailored size were successfully fabricated by an *in-situ* gas foaming in a confined mold followed by freeze-dried. Gas-foamed scaffolds displayed high porosity, rapid water uptake, and stable mechanical properties. While all of the scaffolds exhibited good cytocompatibility *in vitro*; 3DCSS showed better cell seeding efficiency and chondro-protective effect compared to other scaffolds. Besides, 3DCSS scaffolds supported the formation of more mature cartilage-like tissues along with the best repair outcome in a rabbit articular cartilage defect model *in vivo*, as well as less expression level of pro-inflammatory cytokines, including interleukin (IL)-1β and tumor necrosis factor (TNF)-α than that of the other groups. Taken together, 3DCSS may provide an alternative therapeutic option for cartilage tissue repair.

1. Introduction

Articular cartilage injuries, resulting from the acute or repetitive trauma, osteoarthritis or various other joint disorders, pose a substantial burden globally, which may cause permanent disability and discomfort influencing the quality of life [1]. Cartilage has a limited intrinsic healing capacity due to the lack of vascularization and innervation network as well as its isolation from the peripheral circulation. Therefore, cartilage injuries remain one of the most problematic diseases for orthopedic surgeons [2]. A variety of clinical approaches, such as drilling, mosaicplasty, microfracture, and autologous chondrocyte implantation (ACI), matrix-assisted chondrocyte implantation (MACI) have been proposed for

restoring normal joint congruity and minimize further joint degeneration [3,4]. However, none of these techniques has achieved success for the functional cartilage repair owing to the prior surgical procedures, less numbers of donors as well as the low elasticity and toughness of neo-cartilage tissues [5,6]. To overcome the clinical shortage of synthetic cartilage substitutes, cartilage tissue engineering (CTE) has been put forwarded [7].

Since scaffolds play a significant role in CTE, it is essential to engineer an ideal platform exhibiting characteristics, such as biocompatibility, biodegradability, and sufficient mechanical strength to support cell differentiation and matrix production [8]. Numerous strategies have been devised to afford CTE scaffolds, such as phase separation, knitting, 3D printing, and electrospinning; the latter has gathered significant attention of the research

* Correspondence to: M. Shafiq, Shanghai Engineering Research Center of Nano-Biomaterials and Regenerative Medicine, State Key Laboratory for Modification of Chemical Fibers and Polymer Materials, College of Chemistry, Chemical Engineering and Biotechnology, Donghua University, Songjiang, Shanghai 201600, China.

** Correspondence to: Y. Liu, Research Institute of Plastic Surgery, Wei Fang Medical College, Weifang 261000, China.

*** Corresponding author.

E-mail addresses: dr.muhammadshafiq@ucp.edu.pk (M. Shafiq), yuliu1211@163.com (Y. Liu), xmm@dhu.edu.cn (X. Mo).

¹ These authors contributed equally to this work.

community owing to its applicability to a myriad of materials with high nanofiber production efficiency [9–11]. Nonetheless, the morphology of the membranes assembled from normal electrospinning is generally comprised of dense-packed randomly-aligned fiber layers with only superficial pores, impeding cellular infiltration necessary to form 3D tissues [12]. Conjugate electrospinning, which utilizes double metal spinnerets with opposite charges, has been extensively researched to fabricate nanoyarn scaffold manifesting a highly organized structure for annulus fibrosus or vascular tissue engineering [13]. Meanwhile, the simultaneous operation of two nozzles promotes the efficiency of the fabrication process. Although membranes assembled from conjugate electrospinning have achieved some improvements in the topological arrangement and porosity as compared to those fabricated by using conventional electrospinning, the tightly-packed fibers' organization still limits cellular infiltration [14]. Thus, there is a dire need to devise strategies to convert 2D nanofibrous membranes into 3D-like porous structures.

An array of post-treatment methods, such as gas foaming, self-assembly of short fibers, and electrospraying have been proposed for transforming 2D membranes into 3D scaffolds [15,16]. Among, gas foaming, which either utilizes gas bubbles generated *in situ* via a chemical reaction (e.g., the decomposition of sodium borohydride, NaBH₄) or the addition of an inert gas, requires uncomplicated equipment, and can be used in almost all experimental settings, rendering it as an efficient method for fabricating 3D nanofiber matrices with layered structures [17,18]. Although gas-foaming has been widely exploited for fabricating porous scaffolds, the selection of the synthetic material in most of the cases, including the use of hydrophobic polymers, such as nylon, poly(vinylene difluoride) (PVDF), and polycaprolactone (PCL) renders the scaffolds lacking cell recognition cues [19,20]. These scaffolds require further modification by plasma, or coating with extracellular matrix (ECM)-derived proteins or peptides to improve their hydrophilicity and cytocompatibility [21,22]. Alternatively, natural and synthetic materials were combined to prepare hybrid gas-foamed scaffolds for wound healing or nerve regeneration, but how to improve their biological functionality, such as the induction of cell differentiation and promotion of specific cellular matrix secretion is still a challenge [23,24]. It is well-known that the cartilage degeneration exacerbates inflammation in the joints, leading to an overproduction of pro-inflammatory mediators [25]. The establishment of a microenvironment that may promote cartilage proliferation, maintains the cell phenotype as well as attenuates inflammation is therefore highly beneficial for cartilage regeneration. Furthermore, the control of the thickness of gas-foamed scaffold has received only a little attention. It is difficult to precisely control the size of the scaffolds merely by varying the concentration of the foaming medium or the processing time.

In this study, we designed chondroitin sulfate (CS)-crosslinked 3D poly(L-lactide-co-ε-caprolactone)/silk fibroin (PLCL/SF) scaffolds (3DCSS) with precise thickness and evaluated their potential for cartilage regeneration. The SF can enhance the hydrophilicity of the hybrid scaffold and promote cell proliferation, while also possesses a low inflammatory potential [26]. On the other hand, the CS is the physiological component of the cartilage, possessing numerous useful merits, including anti-inflammatory activity, water and nutrients' absorption, and chondrogenic potential at cellular level that helps restore structure and function of the articular cartilage [27]. Briefly, 2D PLCL/SF nanofibrous scaffolds (2DS) were afforded by conjugate electrospinning, followed by crosslinking with the CS by using 1-ethyl-3-(3-dimethylaminopropyl) carbodiimide (EDC) and N-hydroxysuccinimide (NHS). Then, scaffolds were loaded into a manually fabricated mold and immersed into gas foaming solution (sodium borohydride, NaBH₄) to obtain porous 3DCSS with tailored size. We hypothesize that 3DCSS scaffolds feature precise thickness, better biomechanical and biological properties, which concurrently encourage cellular infiltration, chondrification, cartilage-specific ECM matrix secretion, and inflammation resolution. After a thorough characterization, including the composition, morphology, mechanical properties, cytocompatibility, and inflammatory response, the scaffolds were investigated in terms of the chondroinductivity for up to 6 weeks in an *in vitro* culture as well as in an *in vivo* articular cartilage defect model in rabbits (Fig. 1).

2. Experimental

2.1. Materials

Poly(L-lactide-co-ε-caprolactone) (PLCL, M_w = 300 kDa, L-lactide acid to ε-caprolactone mole ratio, 50:50) was purchased by Jinan Daigang Biomaterial Co., Ltd. (Jinan, China). Hexafluoroisopropanol (HFIP) was obtained from Shanghai Darui Fine Chemical Co., Ltd. (Shanghai, China). Cocoon of *B. mori* silkworm was purchased from Huzhou Silk Co., Ltd. (Huzhou, China). Chondroitin sulfate sodium salt (CS, purity, 95%, from porcine cartilage) was obtained from Macklin Biochemical Co., Ltd. (Shanghai, China). Sodium borohydride (purity, ≥98%) was purchased from Sinopharm Chemical Reagent Co., Ltd. (Shanghai, China). 2,2-Diphenyl-1-picrylhydrazyl (DPPH) was purchased from Sinopharm Chemical Reagent Co. Ltd. (Shanghai, China).

2.2. Fabrication of two-dimensional nanofiber mats

A purpose-built electrospinning device (SS-3556H, Ucalery, Beijing, China) with a double-nozzle conjugated electrospinning system was utilized to fabricate two-dimensional PLCL/SF scaffolds (2DS) as described previously [28]. PLCL and SF were dissolved in HFIP in a mass ratio of 8:2 at a total concentration of 10% (w/v). The mixed solution was loaded into two oppositely positioned syringes (10-mL) with blunt-ended 20 G needles and pumped at a flow rate of 1.2 mL/h. A high-voltage with positive (+12 kV) and negative (−12 kV) static current was introduced on the needles on each side. During electrospinning process, the nanofibers carrying opposite charges were intertwined in the air, and a rotating circular drum (500 rpm) was placed between two jets to collect the arranged 2DS.

2.3. Fabrication of 3D PLCL/SF scaffolds and CS-crosslinked scaffolds

Prior to the fabrication of 3D PLCL/SF scaffolds (3DS), 2DS were cross-linked to improve the stability of membranes. 2DS were submerged into 50 mL of mixed cross-linking agent containing 0.49 g (50 mM) of 2-morpholinoethanesulfonic acid (MES), 0.29 g EDC (30 mM), and 0.046 g NHS (8 mM) for up to 6 h. The cross-linked membranes were washed with deionized water three times and then dried in a vacuum oven at 37 °C. Subsequently, 0.38 g of NaBH₄ was added to 20 mL of deionized water to prepare the foaming agent (concentration: 0.5 M). 2DS were immersed into 20 mL foaming agent and removed from the medium at pre-determined time point. After rinsing with the deionized water three times and freeze-drying, the dried porous 3DS was obtained. The production of hydrogen bubbles from NaBH₄ solution is based on the equation (Eq. (1)):



To obtain CS-crosslinked 3D scaffolds (3DCSS), the same cross-linking agent as mentioned above was firstly prepared with the only difference that 1 g of CS (w/v: 2%) was added into the 50 mL of crosslinking agent. 2DS were immersed into the cross-linking agent containing CS for 6 h. Subsequently, free CS and salt on the 2DS were washed with deionized water for three times. After drying, the CS cross-linked 2D membranes were treated with the above gas foaming method and subsequently processed (rinsed and freeze-dried) to afford 3DCSS.

For preparing 3D gas-foamed nanofiber scaffolds with precise controllable thickness, a mold with pre-determined height (3 mm) was employed. Briefly, a concave mold made of hot-poured Teflon was used as a base, and a matching-sized glass was then covered and adhered to the base by using light-curing glue. The electrospun nanofiber mat was placed at the center of the mold and immersed into the NaBH₄ solution as described above. After half an hour, the holder was removed and rinsed thrice with deionized water with the scaffold inside. After freeze-drying, 3DS or 3DCSS with precise thickness were obtained.

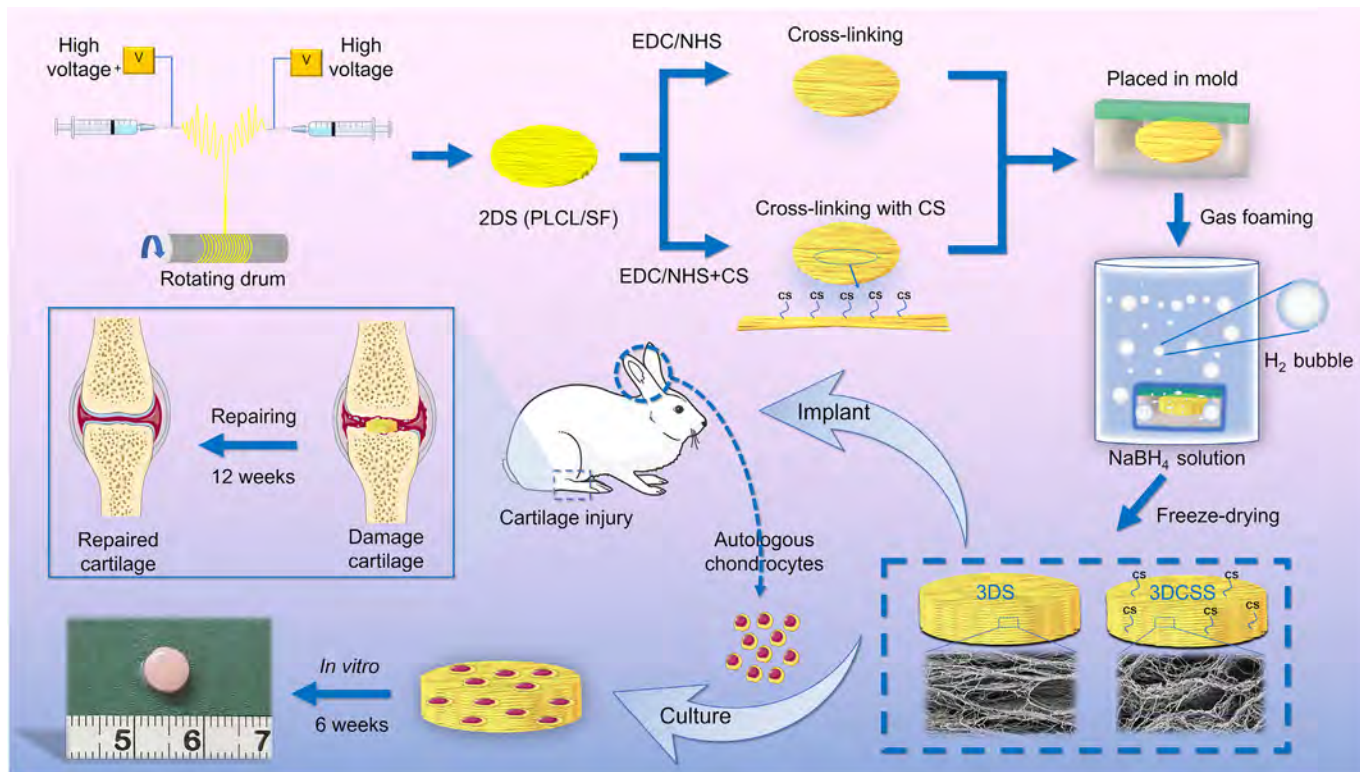


Fig. 1. Schematic illustration of the preparation of 2DS, 3DS, and 3DCSS scaffolds for CTE. 2DS were fabricated by conjugate electrospinning, crosslinked via CS, and expanded by using gas foaming. The bioactivity of membranes was assessed *in vitro* and *in vivo*.

2.4. Characterization

The bulk volume of samples was measured by ethanol displacement method [20]. The volume percentage of specimens (square-shaped, length = 10 mm; thickness = 0.5–7 mm) was then calculated by dividing volume of the gas foamed scaffold at different time intervals with the volume of the initial membrane. The bulk density of specimens was calculated by dividing the mass of specimen with its bulk volume. The porosity of the nanofiber membranes and expanded scaffolds was measured by the liquid displacement method and calculated according to Eq. (2) [29]:

$$P(\%) = \frac{W_s(g) - W_d(g)}{r(g/cm^3) \times V(cm^3)} \times 100\% \quad (2)$$

where P is the porosity, w_s is the weight of the sample after soaking in ethanol for up to 10 min with a density of r , W_d is the weight of the dry scaffold, and V is the volume of the sample ($n = 3$).

The photographs of 2D and 3D gas-foamed scaffolds were recorded by a digital camera (2DS length \times width \times thickness: 10 mm \times 10 mm \times 0.5 mm; 3DS and 3DCSS length \times width \times thickness: 10 mm \times 10 mm \times 3 mm). Samples were mounted on an aluminum stub with carbon tape and then sputter-coated with Au. Scanning electron microscopy (SEM, Phenom XL, Phenom Scientific Instruments Co. Ltd., Shanghai, China) was employed to observe the morphology of different scaffold. SEM images were analyzed by using Image J software to measure the pore area and gap distance of scaffolds. For pore area measurement ($n = 20$), the side length of the different shaped (triangular and diamond) holes was first measured, and then the area was calculated.

The elements on the surface of 3DCSS were analyzed by an energy dispersive spectrometer (EDS, JSM-7500F, China). Structural elucidation of scaffolds was carried out by using Fourier transform infrared spectroscopy (FTIR) with a Nicolet-6700 FTIR spectrometer (Thermo Fisher Scientific, USA) in the range of 3800–600 cm^{-1} .

The antioxidant activity of different samples was assessed by 2,2-diphenyl-1-picrylhydrazyl (DPPH) assay. Briefly, 10 mg of sample (2DS length \times width \times thickness: 10 mm \times 10 mm \times 0.5 mm; 3DS and 3DCSS length \times width \times thickness: 10 mm \times 10 mm \times 3 mm) was mixed with 3 mL of 0.1 mM DPPH/ethanol solution, while protected from the light at room temperature. After reacting for 0.5 h, the absorbance of each mixture was measured at 517 nm using ethanol as the blank. Pure ascorbic acid (AA) was used as a positive control. Whereas, DPPH solution without samples was taken as a blank. Radical scavenging activity of scaffolds expressed as the scavenging rate was calculated by using the following Eq. (3):

$$A(\%) = (A_B - A_S)/A_B \times 100\% \quad (3)$$

where A is the DPPH scavenging rate; A_B and A_S are the absorbance of the blank and experimental samples, respectively.

The water absorption capacity of different samples was determined according to the previous report [30]. The dry sample (2DS length \times width \times thickness: 10 mm \times 10 mm \times 0.5 mm; 3DS and 3DCSS length \times width \times thickness: 10 mm \times 10 mm \times 3 mm) with known weight (w_d) was added into a 25 mL flask containing 20 mL of phosphate buffered saline (PBS, pH = 7.4) solution at room temperature for up to 2.5, 5, and 15 min. Afterwards, the excess water was removed from the scaffolds with a filter paper and the weight of the scaffold was recorded again (w_w). The water absorption rate (w) was calculated according to Eq. (4):

$$w = (w_w - w_d)/w_d \times 100\% \quad (4)$$

where w , w_d , and w_w represent the water absorption rate, dry weight, and weight of scaffold, respectively.

The uniaxial and compressive mechanical properties of scaffolds were measured at room temperature by using a universal materials tester (Instron-5542, Canton, USA). Rectangular-shaped specimens of 2DS (40 mm \times 10 mm \times 0.5 mm), 3DS (40 mm \times 10 mm \times 3 mm) and 3DCSS (40 mm \times 10 mm \times 3 mm) were evaluated by tensile testing in

wet state. A cross-head speed of 5 mm/min was used and specimens were evaluated until their rupture. For the compression test, rectangular-shaped samples with a side length of 10 mm and a thickness consistent with that described above were evaluated at a cross-head speed of 1 mm/min. The stress-strain curves of specimens were drawn by using the data recorded by the machine. Ultimate tensile strength (UTS) and elongation at break (Eb) were determined. The Young's moduli (E) and compressive moduli of scaffolds were calculated analytically by using a slope fitting method of the initial linear region of the stress-strain curves.

For *in vitro* degradation assay, the dry scaffolds (2DS length \times width \times thickness: 10 mm \times 10 mm \times 0.5 mm; 3DS and 3DCSS length \times width \times thickness: 10 mm \times 10 mm \times 3 mm) with known initial weights (W_0) were placed in the 12-well culture plate followed by the addition of PBS (pH = 7.4 \pm 0.1) at 37 °C ($n = 3$). On weekly intervals up to 16 weeks, the scaffolds were removed and dried at room temperature until they gain a constant weight, which was recorded as (W_1). The weight loss (W_L) was calculated according to Eq. (5):

$$W_L = (W_0 - W_1)/W_0 \times 100\% \quad (5)$$

2.5. Evaluation of the biocompatibility of scaffolds *in vitro*

Articular cartilage was derived from New Zealand white rabbit with an approval of the Ethics Committee of Shanghai Pulmonary Hospital and chondrocytes were isolated as previously reported [31]. The chondrocytes were cultured in high glucose, Dulbecco's modified Eagle's medium (DMEM, Gibco, USA) supplemented with 10% fetal bovine serum (FBS, Hyclone, USA) and 1% penicillin/streptomycin/amphotericin B solution in an incubator at 37 °C [32]. Chondrocytes at passage two were used for the subsequent *in vitro* evaluations.

After sterilization by ultraviolet (UV) light for up to 6 h, 2DS (diameter, 14 mm and thickness, 0.5 mm) as well as 3DS and 3DCSS (diameter, 14 mm and thickness, 3 mm) were fixed in the bottom of the 24-well plate, and chondrocytes at a density of 3.0×10^4 cells in 500 μ L of medium were evenly-seeded onto each sample. For initial cell attachment, chondrocytes were incubated for 2 h on the scaffolds before adding culture media to allow for cell attachment and adhesion to the scaffolds. Because the cells were seeded on the scaffolds along with the minimal amount of culture medium, this can maintain the cells' nutritional supply during the initial 2 h. The purpose of this process is to allow more cells distribute throughout the scaffolds, thus reducing the number of cells washed off from the scaffolds due to the addition of culture medium. Live/dead assay was performed by using a live/dead staining kit (In vitrogen, USA). Briefly, after 24 h, cell-seeded scaffolds were rinsed with PBS and incubated in a mixture PBS (200 μ L) solution containing calcein-AM (5 μ M) and propidium iodide (20 μ M) for 15 min at 37 °C in the dark. The fluorescence of cells was observed by using a confocal laser scanning microscope (Nikon, A1RMP, Japan).

The cell seeding efficiency of different scaffolds was analyzed as described previously [33]. The same cell density as above was evenly-dropped onto the scaffolds. After an incubation for up to 4 h, the media from different samples containing unseeded cells were collected and counted (lost cell number). The cell seeding efficiency of different scaffolds was calculated based on Eq. (6):

$$\text{Cell seeding efficiency}(\%) = \frac{\text{total cell number} - \text{lost cells number}}{\text{total cell number}} \times 100\% \quad (6)$$

The proliferation of chondrocytes on scaffolds was determined by a cell counting kit 8 (CCK-8) assay. Chondrocytes (3.0×10^4) were seeded on 2DS, 3DS, and 3DCSS for up to 1, 3, and 7 days in a 24-well plate ($n = 4$). At each time point, the medium was removed and the cell-seeded scaffolds were washed with PBS three times. Thereafter, 200 μ L of medium with 10% CCK-8 reagent was added to each well and incubated for up to 2 h at 37 °C. The absorbance was measured using a microplate

reader (Thermo Fisher Scientific, USA) at the 450 nm for 100 μ L of supernatant per well.

To observe the cell morphology and cell infiltration at pre-determined time points, chondrocytes grown on 2DS, 3DS and 3DCSS were fixed and dehydrated with an ascending series of graded ethanol (30–100%). After drying in the fume hood, the morphology of chondrocytes was examined by SEM.

Dehydrated cell seeded samples were paraffin-embedded, sectioned (5 μ m), and stained by hematoxylin and eosin (H&E). Briefly, sections were stained with Harris hematoxylin solution for 10 min, followed by counterstaining with eosin-phloxine solution for 3 min [34]. Chondrocyte infiltration was imaged by an optical microscope (Leica Microsystems, Germany).

The feasibility of scaffolds in promoting chondrogenesis *in vitro* was further evaluated by combining them with auricular chondrocytes. Firstly, 200 μ L of chondrocytes suspension at a concentration of 3.0×10^8 cells/mL was seeded onto 2DS (diameter, 6.5 mm and thickness, 0.5 mm) as well as 3DS and 3DCSS (diameter, 6.5 mm and thickness, 3 mm). Subsequently, these cell-scaffold constructs were incubated at 37 °C under 5% CO₂ for 2 h and then cultured in chondrogenic medium for up to 6 weeks *in vitro*. For *in vitro* chondrogenesis assessment, high-density chondrocytes (3.0×10^8 cells/mL) were seeded on scaffolds and incubated for 2 h prior to the addition of the culture medium. The chondrogenic medium used in this article was customized medium containing high glucose Dulbecco's Modified Eagle Medium, 10 ng/mL transforming growth factor beta-1 (TGF- β 1, R&D Systems Inc. Minneapolis, USA), 50 ng/mL insulin-like growth factor-I (IGF-I, R&D Systems Inc.), ITS (Insulin-Transferrin-Selenium-X, GIBCO, Life Technologies, Grand Island, N.Y.), ascorbic acid (Sigma-Aldrich, USA), and other supplements (without any serum, all the ingredients of the medium were definable) [35]. The chondrogenic medium changed every 3 days during the culture duration. After 6 weeks, the chondrocyte-scaffold constructs were fixed in 4% paraformaldehyde (PFA) and stained with H&E and Safranin-O. Collagen type II was detected by immunohistochemical staining by following a previous method [36]. For H&E staining, tissue sections were stained with Harris hematoxylin solution for 10 min and counter-stained with eosin-phloxine solution. For Safranin-O/FG staining, tissue sections were stained in fast green (0.05%, w/v) for 5 min, followed by staining in safranin O (0.1%, w/v) solution for 5 min. For immunohistochemical staining of collagen type II, tissue sections were incubated with hydrogen peroxide to block endogenous peroxidase, followed by heat treatment at 60 °C for 1 h to retrieve the antigen. Monoclonal antibodies against type II collagen (ab34712, Abcam; 1:100 dilution) were then added to the scaffolds and incubated overnight at 4 °C, followed by the addition of biotinylated IgG antibodies. After incubation with streptavidin peroxidase, the sections were stained with 3, 3'-diaminobenzidine as the chromogenic agent.

The specimens ($n = 3$) were minced to perform cartilage-related biochemical evaluations for DNA, glycosaminoglycan (GAG), and total collagen content by using PicoGreen dsDNA assay (Invitrogen), dimethylmethylene blue assay (Sigma-Aldrich), and hydroxyproline assay (Sigma-Aldrich) [37]. The cartilage-specific matrices content of cell-scaffold constructs were analyzed. Cartilage samples were digested in proteinase K (1 mg/mL in 50 mM Tris with 1 mM ethylene diamine tetra-acetic acid (EDTA), 1 mM iodoacetamide, and 10 mg/mL pepstatin A; all from Sigma-Aldrich) for 16 h at 56 °C. DNA content was determined by using a total DNA quantification assay (PicoGreen dsDNA assay, Invitrogen, United States) following manufacturer's instructions. Total GAGs content were analyzed by using dimethylmethylene blue assay [37]. Briefly, total GAGs were precipitated by guanidinium chloride solution (0.98 mol/L). After dissolving the GAGs precipitate, the OD values were determined at 595 nm. A standard curve was established using chondroitin-4-sulfate, and total GAGs were determined from the OD value correlating to the corresponding GAGs content in the standard curve. The total collagen content was measured by using a hydroxyproline assay. Samples were prepared by alkaline hydrolysis, and free hydroxyproline hydrolyzates were assayed according to previously described methods [38]. The hydroxyproline content

were finally converted to total collagen content according to the mass ratio of collagen to hydroxyproline of 7.25. To determine the compressive moduli of cell-scaffold constructs ($n = 3$), a biomechanical testing machine (Instron-5542, Canton, USA) was used. Samples were subjected to unconfined compression tests at a strain rate of 1 mm/min until they reached 50% compressive strain. The compressive moduli of samples were calculated based on the slopes of the stress–strain curves.

To explore the changes in the inflammatory response and compare the chondro-protective ability of different scaffolds, chondrocytes were seeded on 2DS, 3DS, and 3DCSS in a 6-well plate with a density of 3.0×10^5 cells/well and treated with interleukin-1 beta (IL-1 β , 10 ng/mL) for up to 24 h. Real-time quantitative polymerase chain reaction (RT-qPCR) was performed to analyze the expression of pro-inflammatory genes, including tumor necrosis factor-alpha (TNF- α), interleukin-1 beta (IL-1 β), and matrix metalloproteinase-13 (MMP13). The total mRNA from cell-laden scaffolds ($n = 3$) were retrieved with TRIzol reagent (Invitrogen, Life Technologies) to extract. About 1 μ g of RNA was used for cDNA synthesis by M-MLV cDNA Synthesis Kit (Promega) according to the manufacturer's instruction. RT-qPCR was performed by using SYBR Green PCR Master Mix (Enzynomics) and ABI StepOnePlus™ Real-Time PCR system (Applied Biosystems). All primer sequences are listed in Table S1 (supplementary information). The expression of all genes was normalized to glyceraldehyde 3-phosphate dehydrogenase (GAPDH) and to gene expression of chondrocytes before seeding into the different samples and the relative expression was calculated by $-2^{\Delta\Delta Ct}$ method.

The expression level of IL-1 β , TNF- α , and MMP13 was analyzed by Western blotting (WB). Briefly, collected cells were lysed with ice-cold radio immunoprecipitation assay (RIPA) lysis buffer (Beyotime, Shanghai, China). The total proteins were extracted and their concentration was measured using a BCA proteins assay kit (Beyotime, Shanghai, China). After electrophoresis, the proteins were transferred onto polyvinylidene fluoride membranes. Then the membranes were blocked and incubated with anti-IL-1 β , anti-TNF- α , anti-MMP13, and anti- β -actin antibody (all purchased from Abcam, USA) at 4 °C overnight. The membranes were subsequently washed with PBS and incubated with horseradish peroxidase (HRP)-conjugated secondary antibodies for 1 h at room temperature. Protein bands were visualized using the enhanced chemiluminescence reagent (Thermo Fisher Scientific, Rockford, IL, USA) and their optical density was determined using Alpha software.

2.6. Assessment of articular cartilage regeneration in rabbits

All animals were performed according to the standard guidelines approved by the ethics committee of Shanghai Jiao Tong University (SJTU). To determine the articular cartilage regeneration capability of engineered scaffolds, 2DS, 3DS, and 3DCSS were prepared prior to surgery. Adult healthy male New Zealand white rabbits, (age, 4 months and weight, 2.5 kg) were randomly selected and divided into three groups ($n = 4$ per group). After anesthesia with 10% of chloral hydrate, cartilage defects (diameter = 4 mm and depth = 3 mm) were created by using a stainless-steel punch on the trochlear groove of the distal femur. The 2DS (diameter = 4 mm and thickness = 0.5 mm) as well as 3DS and 3DCSS (diameter = 4 mm and thickness = 3 mm) were implanted into the defects. Finally, surgical incisions were closed with sutures. Animals were sacrificed at 12 weeks to harvest the knee joint.

The harvested rabbit articular cartilages were firstly observed and scored according to International Cartilage Repair Society (ICRS) macroscopic scoring standard. Thereafter, cartilage samples were decalcified, sectioned, and characterized for histological and further immunohistochemical analysis including H&E, Safranin-O/fast green (Safranin-O/FG), and collagen type I/II staining [36]. H&E, Safranin-O/fast green (Safranin-O/FG), and collagen type II staining procedures were consistent with those described previously. For collagen type I immunohistochemical analysis, tissue sections were incubated with hydrogen peroxide and then incubated in 10% normal goat serum to prevent nonspecific bindings. The slides were then incubated with antibodies against collagen type I (ab34710,

Abcam; 1:100 dilution) for 2 h at room temperature, followed by the addition of biotinylated secondary antibody at 37 °C for 30 min. After incubation with streptavidin peroxidase, the sections were stained with 3, 3'-diaminobenzidine as the chromogenic agent. Furthermore, the regenerated cartilage was also assessed with Modified O'Driscoll histological scoring and Mankin score. The grading and scoring criteria are shown in the Tables S2–S4 (supplementary information). Immunofluorescence staining for IL-1 β and TNF- α was performed on sectioned slices of different groups and the procedures were the same as in Section 2.5. Immunofluorescence staining for the IL-1 β and TNF- α was performed on cartilage sections [39]. Paraffin sections were deparaffinized, rehydrated, and blocked using 4% BSA in PBS for 1 h at room temperature. Then, the sections were incubated with anti-IL-1 β antibody (Abcam; 1:200 dilution) and anti-TNF- α antibody (Abcam; 1:100 dilution) at 4 °C overnight. After washing three times with 0.1% bovine serum albumin (BSA)/PBS, sections were incubated with fluorescent-labeled secondary antibodies (Alexa-Fluor 546 or 488; Abcam; 1:200 dilution). The nuclei were stained with 4',6-diamidino-2-phenylindole (DAPI) (Beyotime, Shanghai, China) for 5 min at room temperature. Imaging was carried out by using a fluorescence microscope (Leica Microsystems, Germany). The synovial fluid was collected by using a 2 mL syringe with an 18-gauge needle and centrifuged at 4000 rpm for 20 min at 4 °C. The supernatants were collected and frozen at -80 °C. The IL-1 β and TNF- α were assayed using enzyme-linked immunosorbent assay (ELISA) by Rabbit IL-1 β ELISA Kit and Rabbit TNF- α ELISA Kit (R&D Systems, USA) according to the manufacturer's instructions. The supernatant (100 μ L) was incubated in a 96-well plate at 37 °C for 2 h. Afterwards, 100 μ L biotinylated antibody specific to IL-1 β or TNF- α was added and incubated for 1 h at 37 °C. After washing with PBS buffer, the sample was incubated with streptavidin peroxidase (100 μ L) for 45 min at room temperature with gentle shaking. After discarding the solution, 100 μ L of 3,3',5,5'-tetramethylbenzidine substrate reagent was added to each well and incubated for 30 min at room temperature in the dark. Subsequently, 50 μ L of termination solution was added to each well, and 450 nm was read immediately.

2.7. Statistical analysis

Experimental data are presented as mean \pm standard deviation (SD). For statistical significance, Student's *t*-test or one-way analysis of variance (ANOVA) with Tukey's post-hoc test was performed where appropriate confidence level. A *p* values <0.05 was considered to be statistically significant (**p* < 0.05, ***p* < 0.01, ****p* < 0.001).

3. Results

3.1. Fabrication and characterization of 2DS, 3DS and 3DCSS

According to the schematic diagram shown in Fig. 1, the fabrication process of 2DS, 3DS, and 3DCSS scaffold can be mainly divided into the four steps: (1) conjugate electrospinning, (2) cross-linking, (3) gas foaming in a confined mold, and (4) freeze-drying. The fabrication of 3D scaffolds is simple and efficient, which is envisaged to be applied to the large-scale industrial processes.

After treatment with NaBH₄ solution for 5 min, the original mats were gradually expanded and the thickness of 3DCSS increased faster than that of the 3DS (Fig. 2A–B). The thickness of 3DS increased from 0.5 mm to 4 mm (Fig. 2C), while it increased from 0.5 mm to 8 mm for 3DCSS (Fig. 2D). The effect of the gas foaming time on the volume expansion, porosity, and density of the expanded scaffolds was further investigated in detail. As shown in Fig. 2E, after 5 min of gas foaming, the volume of the 3DS and 3DCSS was 8 and 18 times larger than that of the unexpanded membranes. The bulk density of the 2D mats was 0.27 g/cm³, which decreased to 0.03 and 0.02 g/cm³ for 3DS and 3DCSS, respectively (Fig. 2F). Similarly, after gas foaming, the porosity increased from 71 to 92% and 69 to 97% for 3DS and 3DCSS, respectively (Fig. 2G). To precisely control the thickness of the 3D scaffold, a mold consisting of a Teflon concave substrate

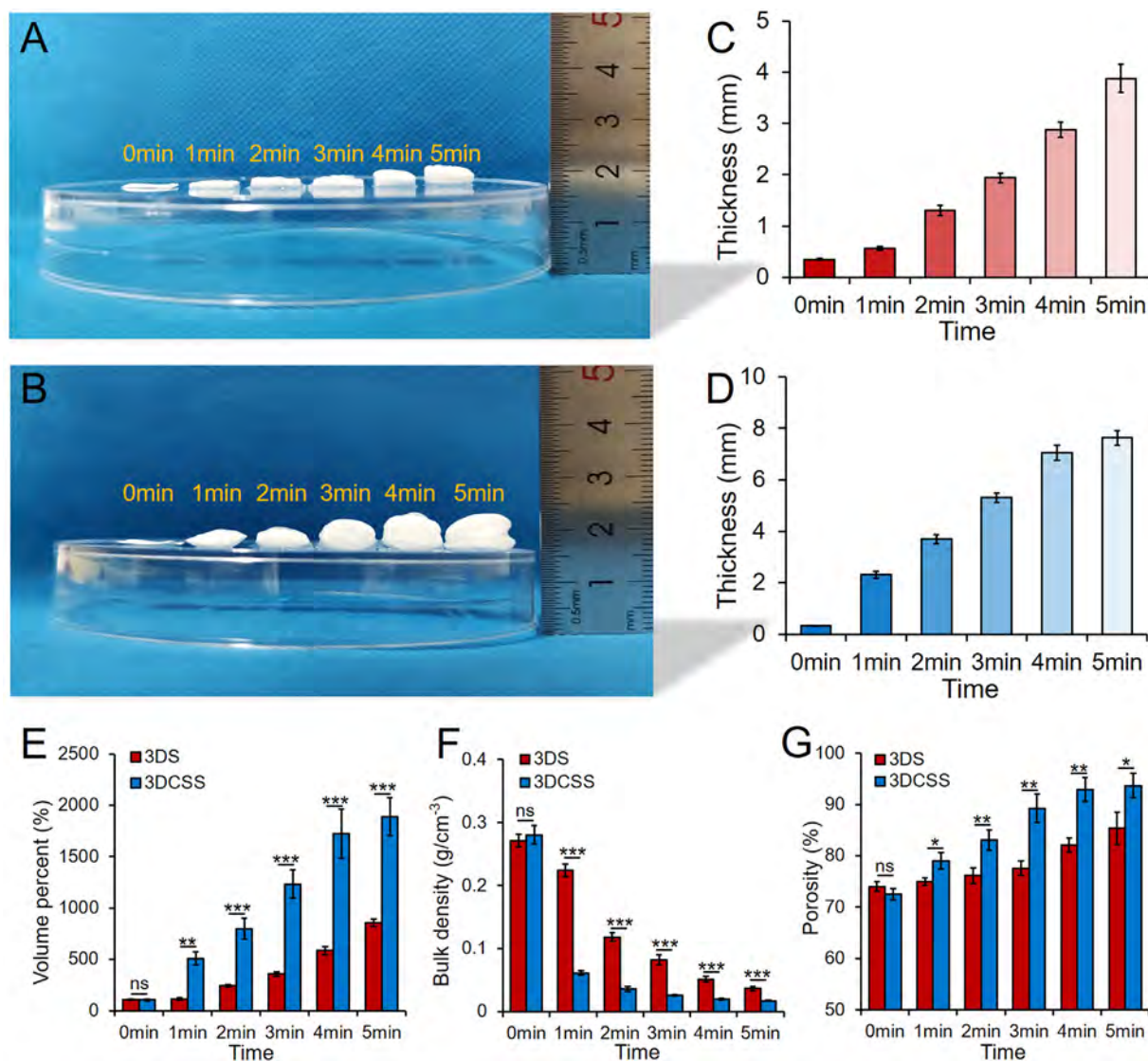


Fig. 2. Photographs of 3DS (A) and 3DCSS (B) before and after expansion for different time intervals. Thickness of the 3DS (C) and 3DCSS (D) for different time points. The volume expansion (E), bulk density (F) and porosity (G) of 3DS and 3DCSS for different time periods. Each value represents the mean \pm SD ($n = 3$). * $p < 0.05$, ** $p < 0.01$, *** $p < 0.001$.

assembled with a matching-sized glass piece was used. Due to the limitation in the height of the mold, the 3D scaffolds stopped expanding when they reached a certain thickness during the foaming process. After freeze-drying, a 3D nanofiber scaffold with a stable and pre-defined thickness was obtained (Fig. 3A). The direction of alignment of scaffolds is shown in Fig. 3B, in which the red arrow indicates the alignment direction of the nanofibers. Fig. 3C exhibited the gross appearance of 2DS with a thickness of 0.5 mm. After expansion in the mold, 3DS and 3DCSS with precise thickness (3 mm) were obtained and the photographs were shown in Fig. 3G and K, respectively. 2DS showed compact-packed structure of the cross-section (Fig. 3D–E) and densely aligned nanofibers and yarns of the surface (Fig. 3F). After expansion, good interconnectivity and continuous layered structure was achieved in 3DS (Fig. 3H–I) and 3DCSS (Fig. 3L–M). In addition, a loose surface with preserved aligned nanofibrous topographical cues was formed in 3D gas-foamed scaffolds (Fig. 3J & N).

The cross-sectional gap distance was also quantified for three types of scaffolds. Prior to the gas foaming, most of gap distances in 2DS were around 3–4 μm (Fig. 3O), which increased to approximately 30–50 μm in 3DS and 30–60 μm in 3DCSS, respectively (Fig. 3P–Q). Moreover, the surface pore areas of 3DS ($64 \pm 20 \mu\text{m}^2$) and 3DCSS ($62 \pm 24 \mu\text{m}^2$) were larger than that of the unexpanded 2DS ($17 \pm 5 \mu\text{m}^2$) (Fig. S1).

The elements on the surfaces of 3DCSS were analyzed by SEM equipped with EDS. The sulfur elements contained in the CS were evenly distributed on the fiber surface of the 3DCSS (Fig. 4A–C). The composition of different samples was further investigated by FTIR and the spectra in the range of 3800–600 cm^{-1} and 2200–600 cm^{-1} are shown in Fig. 4D–E. A strong and wide band at 3435 cm^{-1} was assigned to the OH and NH stretching vibration. The band at 2930 cm^{-1} was assigned to CH stretching vibration, while the shoulder at 1635 cm^{-1} corresponded to the carboxylic (–COOH) groups. Additionally, the stretching vibration of SO of the sulfate groups of the CS was observed at 1255 cm^{-1} [40]. The representative band at 3295 cm^{-1} of 2DS corresponded to the NH stretching vibration of SF, and the bands observed at 1645 cm^{-1} and 1540 cm^{-1} corresponded to the amide I and amide II bonds, respectively. An absorption band at 2938 cm^{-1} was ascribed to the –CH₂– stretching vibration of PLCL. Besides, PLCL exhibited a characteristic band at 1756 cm^{-1} , which is ascribed to the stretching vibration of carbonyl groups of esters. Besides, significant absorption bands appeared at 1454 cm^{-1} and 1359 cm^{-1} , corresponding to the C–H symmetric and asymmetric vibrations, respectively. The gas foaming process does not affect the composition or the chemical interaction among different components of the scaffold, as evidenced by the spectra of 3DS, which exhibits characteristic peaks of SF and PLCL similar to the 2DS.

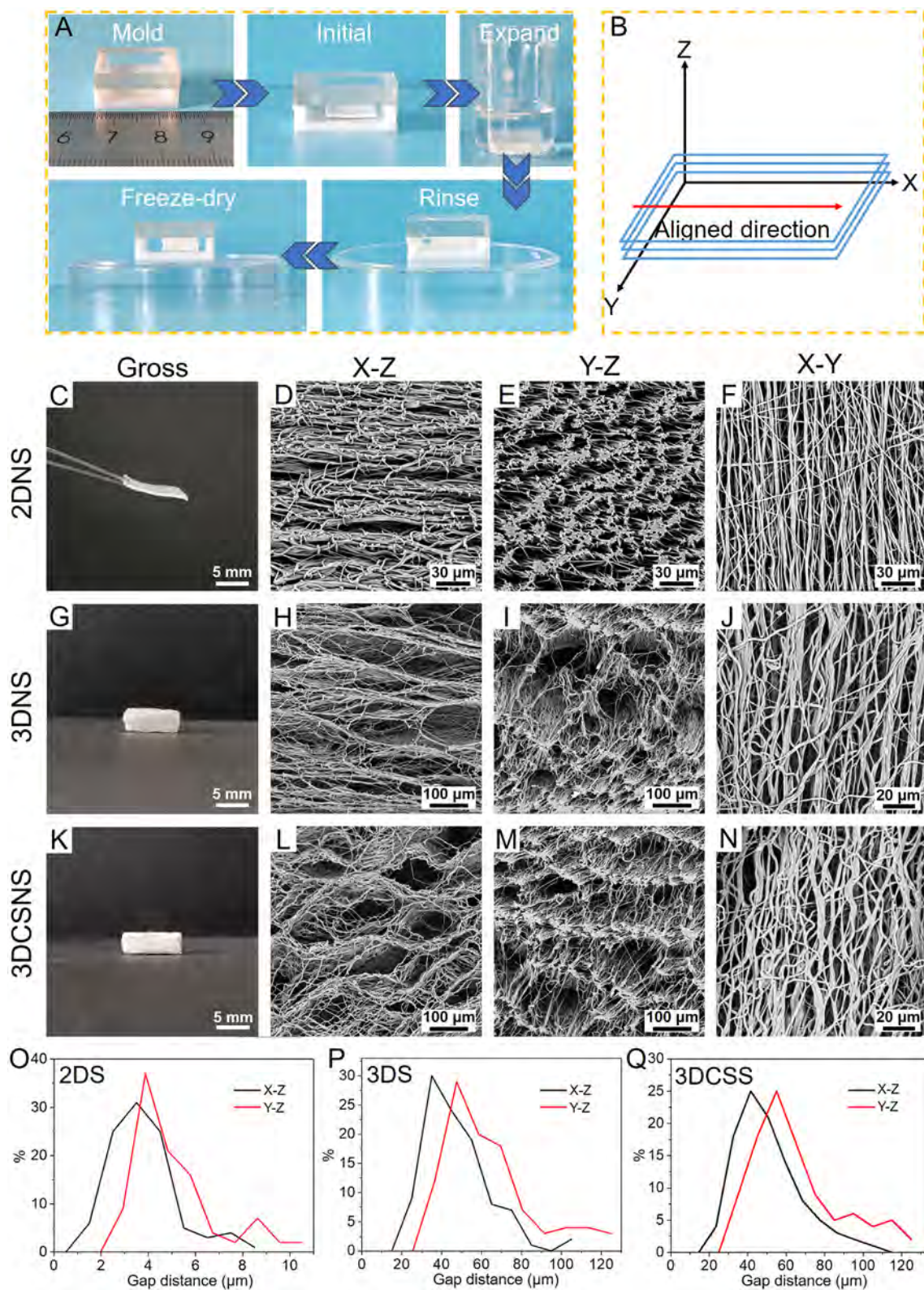


Fig. 3. Fabrication and characterization of gas foamed scaffolds with tailored size. (A) Illustration of the preparation of gas-foamed scaffolds by using a pre-designed mold with 3 mm height. (B) Illustration of the alignment direction of the scaffold. Digital photographs of 2DS (C), 3DS (G) and 3DCSS (K). SEM micrographs of 2DS (D–F), 3DS (H–J), and 3DCSS (L–N). Distribution of the gap distance between the layers of 2DS (O), 3DS (P), and 3DCSS (Q) in different directions.

The introduction of CS resulted into several specific peaks. The band at 3435 cm^{-1} observed in 3DCSS corresponded to the stretching vibrations of OH in the CS. The new amide bond formed by the carboxyl groups of the CS and the amino ($-\text{NH}_2$) groups of the SF by EDC/NHS coupling,

which was confirmed by the shift of the peak of amide II bond from 1540 cm^{-1} toward 1553 cm^{-1} [41,42]. Moreover, an additional carbonyl peak at 1635 cm^{-1} in the 3DCSS spectrum near amide I further indicated the presence of CS in the 3DCSS. Taken together, the FTIR spectra confirmed

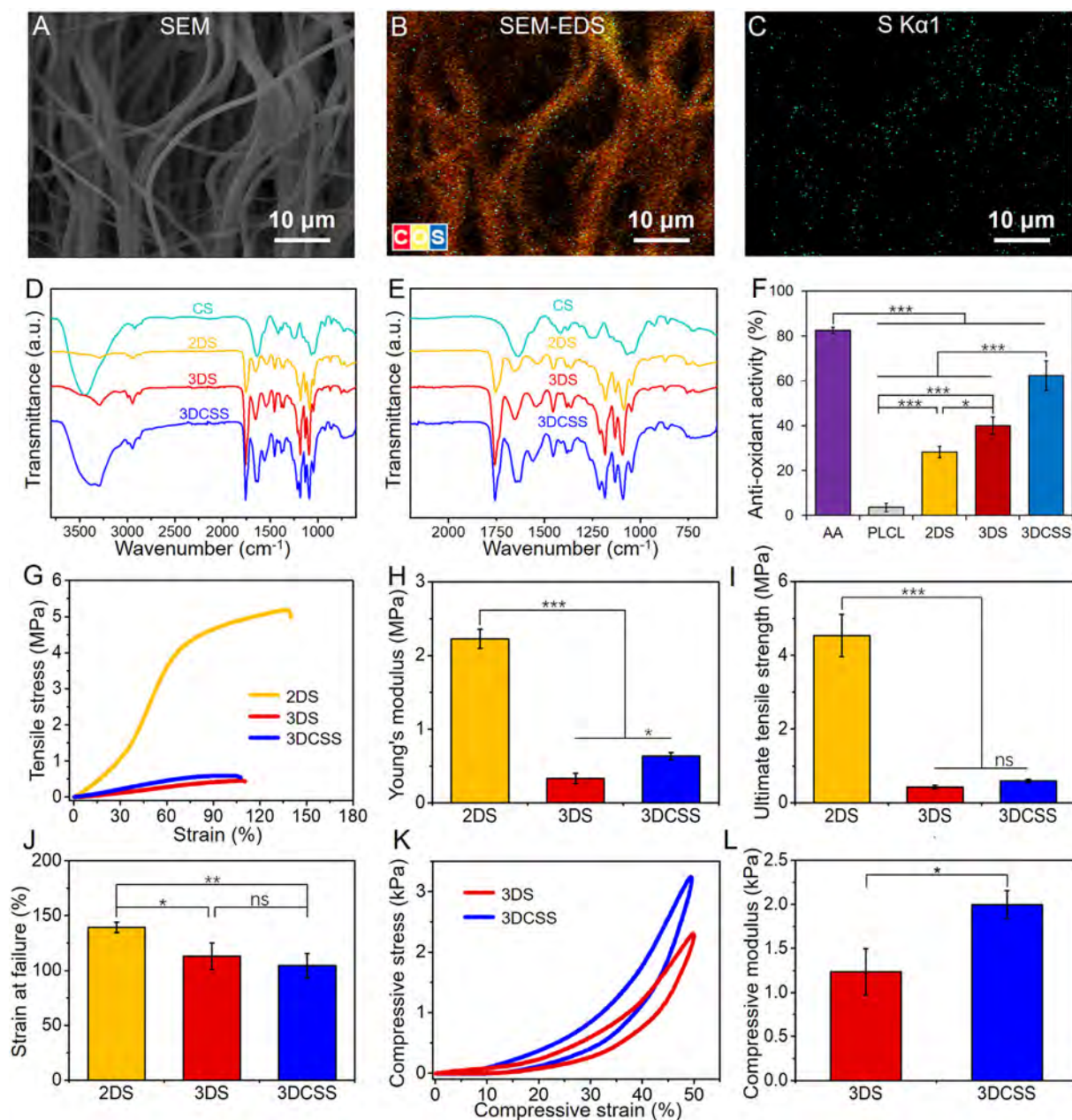


Fig. 4. Representative elemental mapping of the 3DCSS scaffolds including SEM image (A), the EDS image (B), and the distribution of sulfur (C). (D–E) FTIR spectra of CS, 2DS, 3DS, and 3DCSS. (F) Free radical inhibition (antioxidant activity) of PLCL, 2DS, 3DS and 3DCSS by DPPH assay. Representative tensile stress–strain curves (G), Young's modulus (H), ultimate tensile strength (I) and elongation at break (J) of 2DS, 3DS and 3DCSS. Representative compressive stress–strain curves (K) and compressive modulus (L) of 3DS and 3DCSS. Each value represents the mean \pm SD ($n = 3$). * $p < 0.05$, ** $p < 0.01$, *** $p < 0.001$.

the presence of the incorporated components into the scaffolds as well as their crosslinking with the CS.

The antioxidant activity of PLCL, 2DS, 3DS and 3DCSS was analyzed by using DPPH radical scavenging assay. Ascorbic acid was taken as a standard antioxidant. The results were shown in Fig. 4F. The antioxidant activity was found to be 82.49 ± 1.49 , 3.59 ± 1.90 , 28.29 ± 2.52 , 40.04 ± 3.96 and 62.35 ± 6.68 (%) for ascorbic acid, PLCL, 2DS, 3DS, and 3DCSS, respectively.

Fig. 4G exhibited the representative stress–strain curves of 2DS, 3DS and 3DCSS characterized by tensile measurement. The Young's modulus (E), UTS, and Eb of all samples were also summarized (Fig. 4H–J). 2DS exhibited better tensile performance than that of 3D gas foamed scaffolds with E , UTS, and Eb values of 2.22 ± 0.12 MPa, 4.31 ± 0.21 MPa, and $139.21 \pm 4.74\%$, respectively. The E of 3DCSS (0.63 ± 0.04 MPa) was higher than that of 3DS (0.33 ± 0.07 MPa). However, 3DS and 3DCSS

did not significantly differ in terms of the UTS and Eb (3DS, UTS, 0.42 ± 0.05 MPa & Eb $112.96 \pm 12.16\%$ and 3DCSS, UTS, 0.59 ± 0.04 MPa & Eb $104.43 \pm 11.07\%$). Both types of gas-foamed groups exhibited non-linear closed compressive stress–strain curves (Fig. 4L), and the compressive modulus was found to be 1.23 ± 0.26 kPa and 1.99 ± 0.16 kPa for 3DS and 3DCSS, respectively (Fig. 4K). The maximum water absorption of 3DS and 3DCSS scaffolds ($\approx 1800\%$) was reached within 5 min, and was significantly higher than that of the 2DS ($\approx 500\%$) (Fig. S2). The degradation of scaffolds was assessed for up to 16 weeks. The weight loss profiles for the 2DS, 3DS and 3DCSS are shown in Fig. S3. All groups showed almost no change in weight during the first four weeks. By the week 8, the weight loss was $5.7 \pm 0.7\%$, $11.4 \pm 0.6\%$ and $11.2 \pm 0.5\%$ for 2DS, 3DS and 3DCSS, respectively, which increased to $12.7 \pm 0.8\%$, $22.2 \pm 1.3\%$ and $21.2 \pm 0.9\%$ at week 12 and $23.2 \pm 3.2\%$, $37.3 \pm 2.1\%$ and $35.6 \pm 1.8\%$ at week 16. The faster degradation rate of the 3D gas-

foamed scaffold compared to the unexpanded mats may be attributed to the multilayered porous nanofibrous structure of 3D scaffolds with high specific surface area, allowing more nanofibers to trigger hydrolysis reaction with the medium [43].

3.2. *In vitro* cytocompatibility studies

Live/Dead staining assay was used to detect cell viability in the constructs (Fig. 5A–C). Both 2D and 3D gas-foamed scaffolds showed minimal cell cytotoxicity with well-proportioned distribution of chondrocytes after 24 h of culture. More chondrocytes survived on the 3D gas-foamed scaffolds than that of the 2DS. Morphological analysis of chondrocytes at day 5 by SEM showed that they were well-integrated with the scaffolds in all groups and proliferated along the direction of nanofibers (Fig. 5D–F). Besides, more numbers of cells infiltrated into the 3D gas-foamed scaffolds

compared to 2DS as shown by the H&E staining (Fig. 5G–I). Moreover, 3D gas-foamed scaffolds displayed significantly better cell seeding efficiency than that of the 2DS after 4 h of culture *in vitro* (Fig. 5J).

The CCK-8 assay demonstrated that all nanofiber scaffolds had good cell viability *in vitro* (Fig. 5K). From day 1 to 7, the proliferation of chondrocytes on the 3D gas-foamed scaffolds was significantly higher than of the 2DS. Notably, at day 7, the 3DCSS showed the highest numbers of cells among all of the investigated groups. Taken together, these results reveal that 3DCSS could provide a conducive environment for cell growth and infiltration *in vitro*, which may also have implications for the *in vivo* applications.

3.3. Cartilage regeneration *in vitro*

To further validate the regenerative ability of engineered scaffolds *in vitro*, chondrocytes were evenly dropped onto different scaffolds and

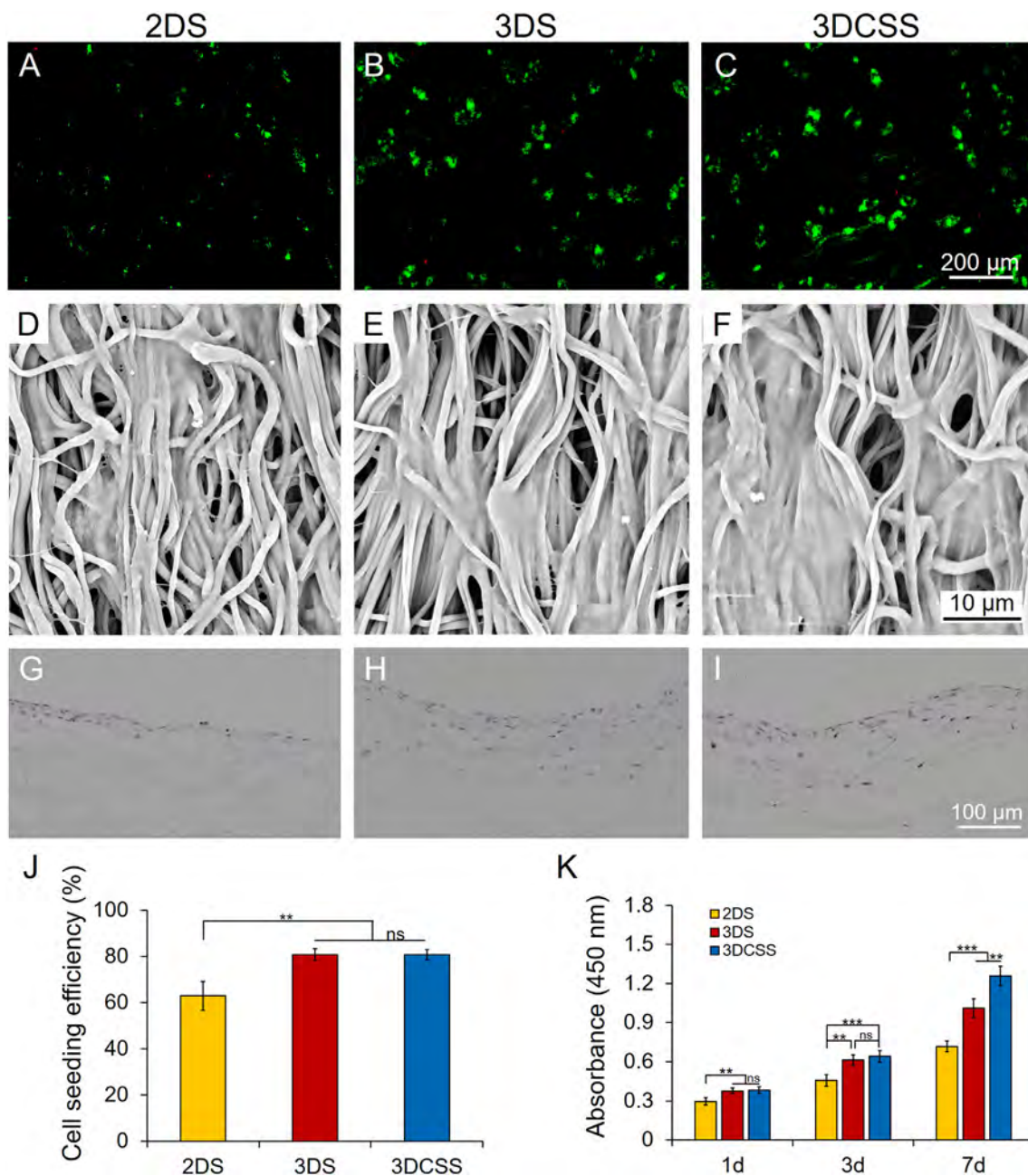


Fig. 5. Live/dead staining of chondrocytes seeded on 2DS (A), 3DS (B), and 3DCSS (C) after 24 h of culture. SEM images of chondrocytes on 2DS (D), 3DS (E), and 3DCSS (F) after 5 days of culture. H&E staining of infiltrated chondrocytes in 2DS (G), 3DS (H), and 3DCSS (I) after 7 days of culture. (J) Cell seeding efficiency of 2DS, 3DS, and 3DCSS after 4 h of culture ($n = 3$). (K) Proliferation of chondrocytes on 2DS, 3DS, and 3DCSS at day 1, 3, and 7 ($n = 4$). * $p < 0.05$, ** $p < 0.01$, *** $p < 0.001$.

grown for up to 6 weeks. All of the scaffolds, maintained their circular shapes and presented cartilage-like tissue development surrounding the construct (Fig. 6A–C). H&E staining results revealed that the specimens in both 3DS (Fig. 6E) and 3DCSS (Fig. 6F) groups presented the formation of lacuna-like cartilage structure. The regenerated tissues in the 3DS and 3DCSS were loose; however, connected and densely-distributed

chondrocytes were observed in 2DS specimens, and some of them showed fibrocartilaginous characteristics (Fig. 6D). On the other hand, 2DS and 3DS specimens exhibited positive staining for Safranin-O and collagen type II only in some regions of the regenerated cartilage (Figs. 6G–H & S4A–B). 3DCSS exhibited a relatively dense and homogeneous distribution of cartilaginous tissues than that of the 2DS and 3DS groups (Figs. 6I & S4C).

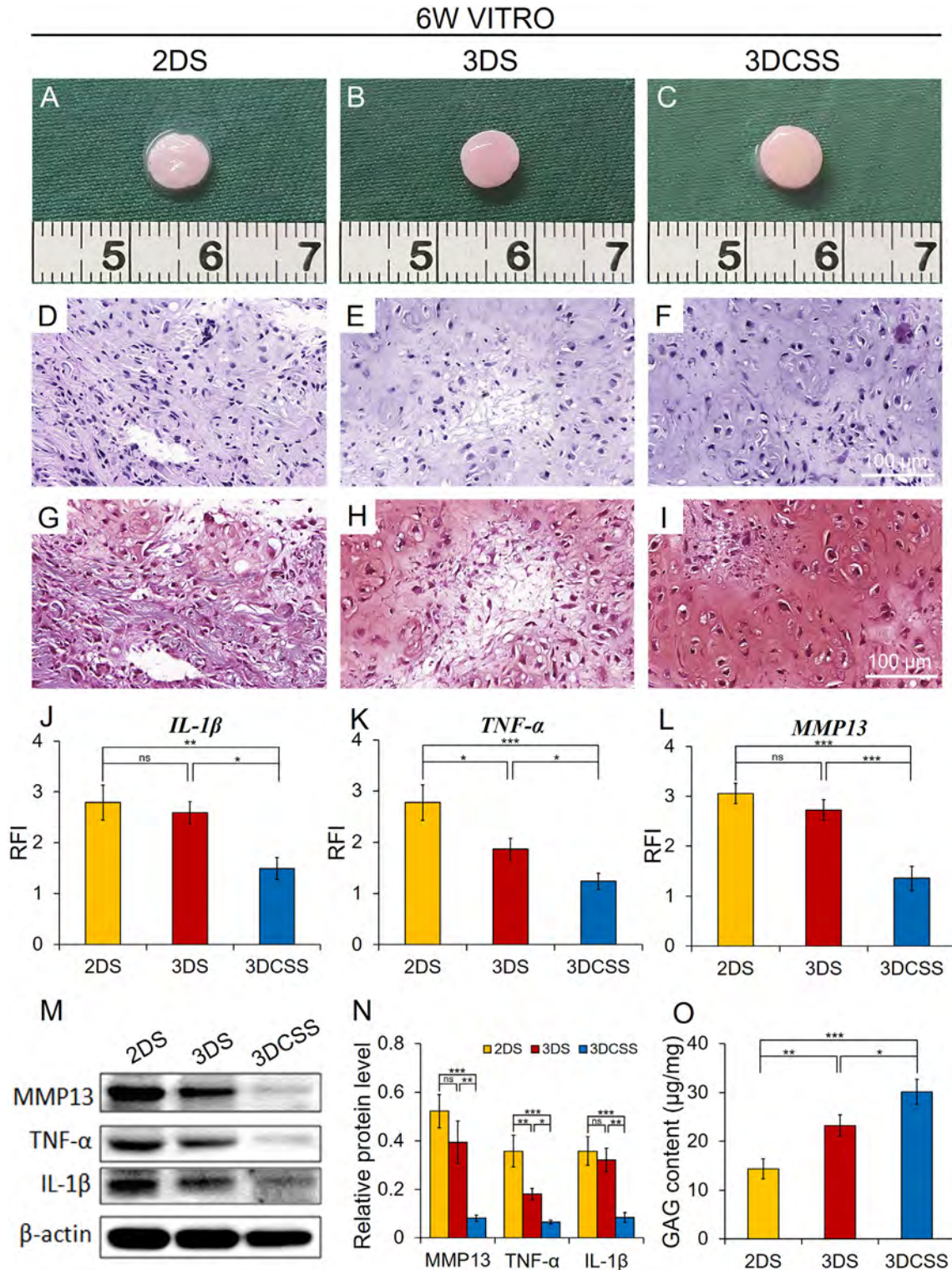


Fig. 6. Macroscopic images (A–C), H&E staining (D–F), and Safranin-O staining (G–I) of engineered neo-cartilage after 6 weeks of culture *in vitro*. Real-time PCR detection of inflammatory factors, including IL-1 β (J), TNF- α (K), and MMP13 (L) in chondrocytes cultured on different scaffolds ($n = 3$). (M) Western blotting assay of IL-1 β , TNF- α , MMP13 and β -actin and (N) the corresponding protein levels in chondrocytes cultured on different scaffolds ($n = 3$). (O) Biochemical analysis of GAG content of cell-scaffold constructs after 6 weeks of culture *in vitro* ($n = 3$). RFI = Relative fold induction. Each value represents the mean \pm SD. * $p < 0.05$, ** $p < 0.01$, *** $p < 0.001$.

To ascertain the chondro-protective ability of different scaffolds, chondrocytes were seeded on scaffolds and treated with IL-1 β to mimic the inflammatory microenvironment after injury. The transcription of inflammatory genes was also evaluated by RT-qPCR (Fig. 6J–L). As anticipated, the inflammatory genes, such as IL-1 β , TNF- α and MMP13 were only marginally detected in the 3DCSS group than that of the other groups. Moreover, Western blot analysis also showed significantly lower expression levels of IL-1 β , TNF- α and MMP13 on chondrocytes-seeded 3DCSS scaffolds than that of 2DS and 3DS groups (Fig. 6M–N), confirming the better anti-inflammatory effect of 3DCSS *in vitro*. The quantitative analysis showed that the compressive modulus (Fig. S5A), DNA content (Fig. S5B), total GAG content (Fig. 6O), and collagen content (Fig. S5C) were higher in 3DCSS as compared to the other groups, indicating that the 3DCSS were conducive in terms of matured cartilage regeneration and cartilage-specific matrix production than that of the other scaffolds.

3.4. Articular cartilage regeneration in vivo

Cartilage regeneration *in vivo* was a crucial criterion to determine the appropriateness of the scaffold for CTE. A rabbit articular cartilage defect model was used to assess the reparative capability of 2DS, 3DS and 3DCSS. After implantation for up to 12 weeks, the gross appearance of retrieved articular cartilage tissues was ascertained. The cartilage defects in the 2DS groups were clearly visible, indicating the poor integration of the scaffolds with the native cartilage tissues (Fig. 7A). Similarly, the defects were only partially covered by the newly-formed cartilage-like tissues in the 3DS group (Fig. 7B). By contrast, implantation of 3DCSS displayed significantly better formation of neo-cartilage, which accumulated the defect site and integrated well with the native cartilage tissues; the boundary between the defect site and the host cartilage was almost invisible (Fig. 7C).

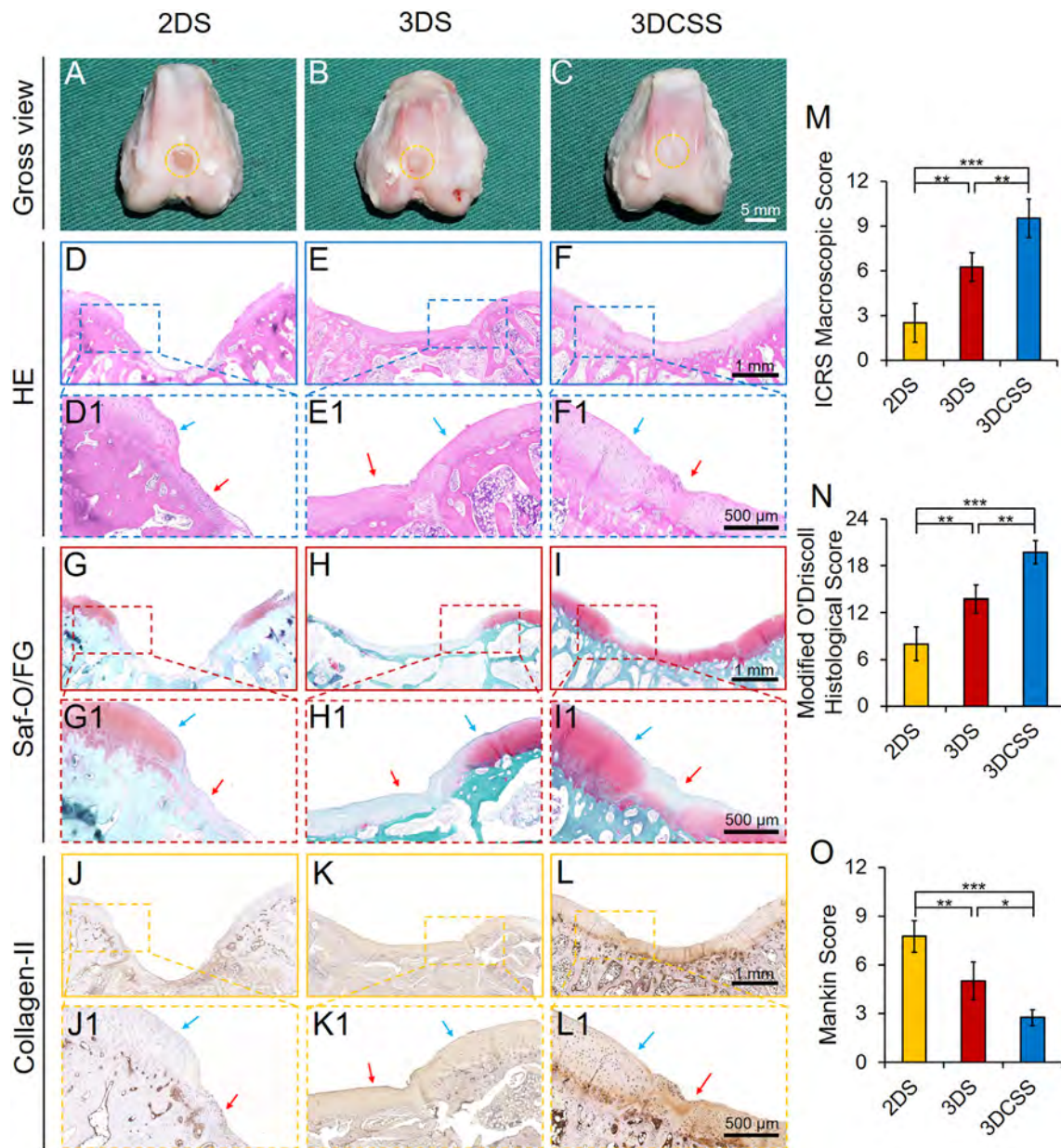


Fig. 7. (A–C) Macroscopic images of cartilage joints of cartilage defects regions at 12 weeks post-surgery, H&E (D–F, D1–F1), Safranin-O/FG staining (G–I, G1–I1), and type II collagen (J–L, J1–L1) immunohistochemical staining of regenerated cartilage defects in different groups 12 weeks after surgery. The blue arrows point toward the intact cartilage area, and the red arrows indicate the cartilage defect area. ICRS macroscopic assessment score (M), modified O'Driscoll histological score (N) and Mankin score (O) of the repaired tissue. Each value represents the mean \pm SD ($n = 4$). * $p < 0.05$, ** $p < 0.01$, *** $p < 0.001$.

H&E staining and Safranin O-fast green staining assays of the retrieved cartilage samples were further performed to examine the formation of fibrous tissue, and the deposition of ECM. In 2DS groups, an irregular border between the neo-tissues and native cartilage was observed with only fibrous tissues filling the defect; only a few unevenly distributed cartilage clusters filled the defect (Fig. 7D & D1). For the 3DS, a thin layer of cartilage-like tissue was observed on the surface of the defect region, whereas some fibrous tissues containing fewer cells were found (Fig. 7E & E1). By contrast, the 3DCSS groups displayed a well-integrated boundary filled with homogeneously distributed newly formed tissues featured with the chondrocyte-specific lacunas (Fig. 7F & F1).

2DS group also lacked Safranin O-fast green staining in the defect region (Fig. 7G & G1). For 3DS groups newly formed tissue with a weak staining for the Safranin O-fast green filled the defect region (Fig. 7H & H1). These results indicated that 2DS and 3DS groups exhibited fibrous tissue, which lacked the deposition of the cartilage-specific ECM. Alternatively, 3DCSS groups exhibited the substantial formation of positively-stained cartilage ECM, indicating the formation of matured cartilage as well as the deposition of the abundant GAGs (Fig. 7I & I1). The immunohistochemical analysis of the collagen type II also showed a significant deposition of the collagen type II (Fig. 7L & L1) in 3DCSS groups compared to 2DS (Fig. 7J & J1) and 3DS (Fig. 7K & K1), which displayed only a minute deposition of collagen. While 3DCSS groups showed only a weak staining for the

collagen type I; the 2DS showed the substantial formation of collagen type I; 3DS groups exhibited only a few regions containing collagen type I (Fig. S6). All of these results demonstrated that 3DCSS achieved a satisfactory regeneration of cartilage along with the accumulation of the cartilage-specific ECM rather than the fibrocartilage formation.

To evaluate the quality of the regenerated cartilage, the results of ICRS macroscopic score (a total 12 points), modified O'Driscoll histological score (a total 24 points) and Mankin score (a total 14 points) were summarized. 3DCSS groups showed better ICRS macroscopic score (10.2 ± 0.9), significantly higher than that of the 3DS (7.0 ± 0.8), and 2DS groups (5.2 ± 0.9) (Fig. 7M). A similar trend was observed in the modified O'Driscoll histological scoring, in which 3DCSS exhibited the higher score (20.5 ± 1.9) than that of the other two groups (14.0 ± 1.8 for 3DS and 9.7 ± 1.5 for 2DS) (Fig. 7N). Mankin score further indicated the best repair outcome in 3DCSS group (2.75 ± 0.5) compared to 3DS (5 ± 1.15) and 2DS (7.75 ± 0.95) (Fig. 7O).

The intra-articular inflammatory response was discerned by immunofluorescent staining for different types of inflammatory markers, which demonstrated a high expression of IL-1 β and TNF- α in the 2DS group as compared to the other groups. Similar to the native cartilage, weak fluorescent expression of pro-inflammatory markers was observed in 3DCSS groups (Fig. 8A). Meanwhile, quantification results of inflammatory factors, such as IL-1 β and TNF- α , showed the less expression of inflammatory

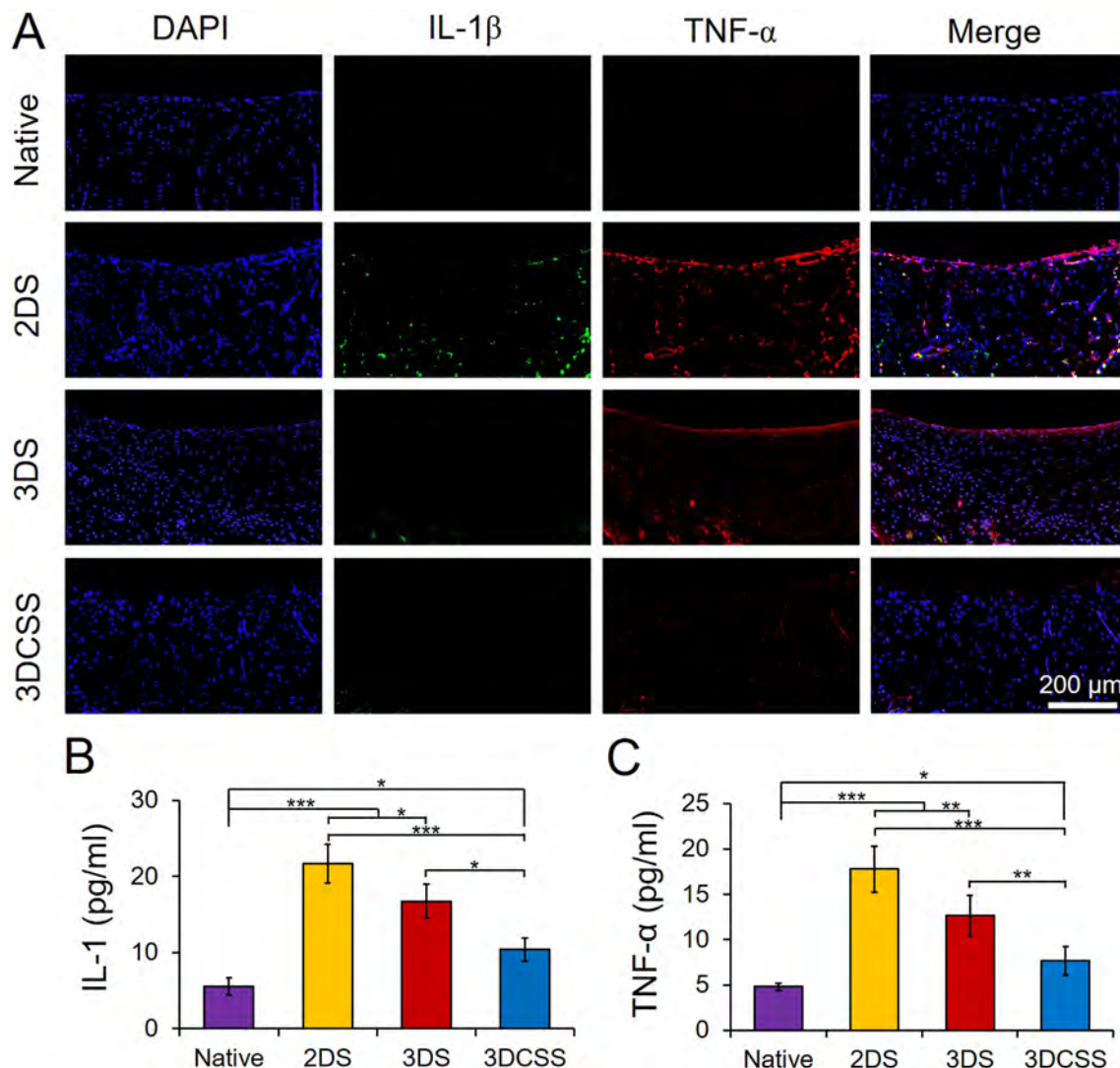


Fig. 8. (A) Immunofluorescent staining for IL-1 β and TNF- α of the defect regions 12 weeks post-surgery. Quantification of concentration of IL-1 β (B) and TNF- α (C) in the joint fluid using ELISA kit. Each value represents the mean \pm SD ($n = 4$). * $p < 0.05$, ** $p < 0.01$, *** $p < 0.001$.

markers in the 3DCSS groups compared to the 2DS and 3DS groups, indicating that 3DCSS attenuated the inflammatory response and provided a conducive environment for neocartilage formation (Fig. 8B–C).

4. Discussion

Electrospinning, as a universal and a cost-effective nanofiber fabrication technology, has been extensively explored for the fabrication of tissue engineering scaffolds and devices for a myriad of clinical and industrial applications [44]. However, it is known that 2D nanofiber membranes generated by conventional electrospinning pose certain restrictions for cell infiltration due to their tightly-packed layers and dense superficial pores, which lack 3D-like architecture for tissue regeneration. Recent studies reported numerous attempts to afford 3D tissue-engineered scaffolds with nanofibrous structures based on 3D printing or self-assembly of short nanofibers as well as self-folding nanofiber mats [33,45,46]. Besides, it has been reported that the porosity and pore size of electrospun scaffolds can be tailored by varying the fiber size [47,48]. These technologies are limited by some constraints, such as exposure of the scaffolds to the toxic solvents, lengthy and time-consuming preparation procedures as well as the requirement of the special instrumentation. Alternatively, the gas foaming technique, has been frequently exploited for the post-treatment of electrospun nanofiber membranes to afford 3D nanofiber scaffolds. Gas foamed scaffolds often feature laminated fibrous layered structure with high porosity and interconnected pores, providing sufficient space and a stable 3D-like architecture for cell infiltration and proliferation [17,19]. However, to the best of the authors' knowledge, most of the gas-foamed scaffolds have been assembled from synthetic polymers, such as poly(caprolactone) (PCL), poly(L-lactide-co- ϵ -caprolactone) (PLCL), or poly(L-lactide) (PLLA), which lack cell recognition cues, and necessitate post-modification with ECM-derived proteins or peptides for tissue repair applications. Moreover, merely by adjusting the physical parameters, such as time or the concentration of the foaming agent to afford scaffolds with the controlled structure and size may not hold considerable potential to achieve uniform expansion throughout the scaffold, especially in the central region [21,49]. To circumvent these limitations and afford 3D-like nanofibrous scaffolds, herein, we realized bio-hybrid scaffolds by converging electrospinning and gas foaming, namely, 3DCSS which exhibited 3D-like multilayered nanofibrous structures with adjustable size and antioxidant properties for articular cartilage regeneration applications. The porous 3DCSS possessed low density, high porosity, good mechanical properties, biocompatibility and antioxidant capacity. Furthermore, the CS-crosslinking further improved the chondrogenic potential of the gas foamed scaffolds, translating into better cartilage formation *in vitro* and *in vivo*. Compared with our previous report on gas foamed PLCL/SF scaffolds [50], CS was introduced to endow chondrogenic and antioxidative potential to scaffolds, thus improving their bioactivity and broadening their applicability. It is noteworthy to mention here that while CS-SF based scaffolds have been developed previously and leveraged for cartilage tissue repair, their poor mechanical properties and limited choice of biomaterials may limit their potential [10]. On the other hand, our approach of exploiting natural/synthetic polymer-based hybrids and leveraging electrospinning and gas foaming could help tune scaffolds' dimensions to encourage cellular infiltration and neo-tissue formation.

Appropriate choice of the materials is the basis for the successful preparation of 3D nanofiber scaffolds. Both PLLA and PCL are biocompatible and biodegradable, which have been widely used for an array of biomedical applications. However, PLLA-based scaffolds produce acidic byproducts upon their hydrolysis *in vivo*, which may cause acid-induced chronic inflammation [51]. Besides, being highly stiff, PLLA based scaffolds may not be suitable for CTE. On the other hand, the higher flexibility of PCL limits its applications for hard tissue repair [52]. The PCL also degrades slowly, which necessitates the modification of its chemical composition by blending the other polymers or copolymerizing other monomers to regulate its degradation rate and mechanical properties [53]. Alternatively, PLCL is a mechano-elastic biodegradable polymer, whose degradation rate and

mechanical properties can be tuned by varying the monomers' ratio and molecular weight. Moreover, being mechano-elastic, PLCL can promote tissue repair by cellular mechanotransduction, which has already been exploited for soft tissue regeneration, including infarcted heart, blood vessels, and skin [36,54–57]. Kim et al. reported better cartilage ECM secretion and regeneration by PLCL scaffolds. The authors speculated that this may be ascribed to the mechanical elasticity of PLCL promoting cartilage regeneration via cellular mechanotransduction [58]. Consequently, to leverage these characteristics for cartilage tissue regeneration, we chose PLCL as the main component of the scaffold, which may concurrently leverage mechanical properties, biodegradation, and cellular mechanotransduction. Similarly, SF, a protein-based natural polymer contains ligands that can be recognized by the cell-surface receptors, which may improve the biocompatibility of scaffolds [7,59]. The SF exhibits unique properties, such as good biocompatibility and biodegradability, which may also increase the hydrophilicity of the scaffold and overcome the limitations associated with the hydrophobicity of PLCL which may constrict expansion during gas foaming [60,61]. Besides, SF is less risky in terms of the infection compared to the other proteinaceous materials [13]. Hence, a blend of PLCL and SF was employed for the fabrication of scaffold, which has already been exploited for the regeneration of other types of tissues, such as tendons, skin, blood vessels, and nerves [62]. Despite these obvious merits, the applicability of PLCL/SF scaffolds is still limited for CTE, especially in promoting cartilage ECM secretion and alleviating inflammation, which has been addressed by various approaches. Kartogenin-conjugated amphiphilic polyurethanes nanoparticles promoted chondrogenic differentiation of stem cells, however, its use may be limited due to its solubility in the oil, which may not be conducive for functionalization [63]. Similarly, while cartilage-decellularized matrix has been reported to promote cartilage regeneration, immunological risks and difficulties associated with its incorporation into scaffolds may hinder its applications for CTE [48]. Herein, CS, the integral component of the cartilaginous ECM was exploited to endow the bioactivity to PLCL/SF scaffolds and to modulate the inflammatory microenvironment after injury [64]. The CS, a negatively-charged polysaccharide is widely distributed in the cartilage, which is involved in various physiological activities, such as cell growth and differentiation as well as the regulation of the joint function [65,66]. However, the weak mechanical properties of CS may limit its applications for CTE, which require further improvement to harness its benefits for tissue-engineered scaffolds [67,68]. The CS was incorporated into PLCL/SF scaffolds through EDC/NHS crosslinking, which improved chondrogenic induction *in vitro* as well as cartilage regeneration *in vivo*. Our approach of the incorporation of CS into PLCL/SF scaffolds via cross-linking rather than the direct blending during electrospinning is based on different merits. While both the SF and PLCL can afford electrospun nanofibers with the high efficiency, the electrospinning of CS along with scaffolds may impede the efficiency as well as perturb the nanofibers' morphology due to the formation of a bead-like morphology [69–71]. The electrospinning of CS containing scaffolds is further constricted by the limited choice of solvents (e.g., acetic acid, trifluoroethanol/water, HFIP/water etc.). The bead-like morphology of CS-contained scaffolds may further affect the applicability of scaffolds.

The 3DCSS gas-foamed scaffolds also feature additional advantages over other forms of CS-SF related scaffolds. Since, most of the CS-SF scaffolds were fabricated by freeze-drying, the size and shape of the scaffolds may not be appropriately controlled due to the limitations associated with the mold as well as the limited choice of materials [10,72–75]. Alternatively, 3DCSS were prepared by gas foaming, which allowed a better control over shape of 3D scaffolds. The thickness of 3D scaffolds could also be tailored by adjusting the foaming time or mold dimensions [76]. Besides, 3DCSS exhibited a multilayered nanofibrous structure and the layer distance could be controlled by regulating the thickness of the scaffold [77]. Lastly, gas foamed scaffolds are applicable to a wide range of materials, including synthetic polymers, such as PCL, PLCL, and PLA as well as natural polymers (e.g., SF, chitosan, cellulose etc.), which also extend fabrication flexibility [9].

However, the introduction of CS increased the hydrophilicity of the scaffolds, leading to a more rapid increase in the thickness during gas foaming process, posing a challenge to afford 3D electrospun nanofibrous scaffolds with controllable size. To circumvent this limitation and gain a further control over size of 3D electrospun scaffolds, various approaches have been put forwarded. Sun et al. [78] fabricated hexagonal-shaped 3D nanoyarn scaffolds by using a conductive mold, which were mineralized for bone regeneration. Chen et al. [79] employed short nanofibers based bio-inks to prepare 3D printed scaffolds with controllable pore size. In addition, origami- and kirigami-based techniques may offer an alternative to transform electrospun membranes into 3D structures [47]. Despite these possibilities to design 3D scaffolds with accurate size, the superficial pores along with a lack of porous layered structures are an impediment. Herein, we leveraged a simple mold made of Teflon and glass, which is cost-effective, chemically inert, and easy to be assembled. After gas foaming by using this “confined expansion” molding technology, 3D scaffolds with customized thickness and multi-layered structure were generated (Fig. 3).

The high porosity is a fundamental characteristic that enables scaffolds to provide adequate space for cell infiltration. During the gas foaming process, bubbles converge within the nanofiber pores and exert pressure on the surrounding fibers, resulting in an increase in the porosity, which is macroscopically manifested as an increase in the volume and thickness of scaffolds. A highly porous scaffold with an interconnected pore network is required for uniform spatial distribution of cells and to minimize the diffusion-limiting effects on nutrients and waste products [59]. This is particularly essential for high-density chondrocyte culture *in vitro* to produce clinically significant volume of cartilage tissues. Furthermore, high porosity and aligned topographical cues facilitate efficient intercellular contact, which has been associated with the high rates of the ECM synthesis [80]. After foaming and freeze-drying, the 3D gas-foamed scaffolds retain their aligned nanofiber morphology with higher porosity, indicating their better performance over the conventional nanofibrous membranes in promoting cell infiltration and cartilage-related ECM secretion. Furthermore, an ideal scaffold should be able to withstand the specific strength. The mechanical properties of 3DCSS were significantly better than that of 3DS as evaluated both by tensile and compressive tests, which may be due to the formation of strong hydrogen bonds between the CS or the formation of amide bonds between the amino groups and the carboxylic groups.

The biocompatibility and bioactivity of scaffolds are important issues which strongly affect the feasibility of cartilage regeneration. Our results showed that chondrocytes stably survived on all of the scaffolds, indicating good biocompatibility and low cytotoxicity of both 2D membranes and 3D gas-foamed scaffold. Notably, 3DCSS achieved most rapid proliferation of chondrocytes as compared to the other groups and formed uniform cartilage-like tissues along with the secretion of the cartilaginous matrix both *in vitro* and *in vivo*. The biochemical results of chondrocytes cultured on different samples reemphasized the favorable influence of 3DCSS groups on the chondrogenic phenotypes *in vitro* (Fig. 5). This is ascribed to the reason that the 3DCSS scaffolds mimic the GAG-rich ECM of chondrocytes, which may provide the cultured cells with a niche-like microenvironment, allowing them to maintain the differentiated chondrogenic phenotype *in vitro* [81]. Although the mechanical properties of the scaffolds inevitably declined after gas foaming owing to the increased porosity and a loose structure, the 3DCSS showed improved mechanical parameters than that of the 3DS. This may help to present a stable 3D environment for the growth of chondrocytes and cartilage tissue regeneration. The introduction of CS also played a crucial role in enhancing the bioactivity of scaffold. The precise role of CS in creating a chondro-inductive environment for the neo-cartilage regeneration is not very clear. Previous studies have shown that chondrocytes cultured on CS-modified chitosan membranes retained their phenotype and produced cartilage-specific matrix [81]. In another study, the introduction of CS downregulated the expression levels of genes encoding proteolytic enzymes involved in cartilage degradation, suggesting that CS may exert both chondro-protective and anti-inflammatory effects, which may be beneficial for CTE [82]. Consistent with these previous

results, 3DCSS scaffolds showed the bioactivity in promoting the maturation of chondrocytes, formation of a lacuna-like structure and secretion of the cartilage-specific ECM as compared to the CS-free groups both *in vitro* and *in vivo*. The incorporation of CS might have multiple functions, such as the sequestration of the growth factors (GFs) or the direct interaction with the cells. The interaction of growth factors with anionic domains in GAG, of which CS is a primary component, is well-known to play an essential role in morphogenesis and tissue homeostasis [83]. These interactions have been reported to extend the half-life and preserve the activity of GFs [27]. Therefore, it can be assumed that the sulfate domains of CS may interact with some of the GFs, thereby activating the required signaling that may favor cartilage regeneration, thus promoting chondrocytes maturation as well as encouraging the further deposition of cartilage-specific ECM.

Moreover, the antioxidant capability of CS is also important in reducing cartilage matrix degradation and promoting cartilage regeneration. The CS has been shown to scavenge reactive oxygen species (ROS), restore chondrocytes homeostasis, and down-regulate the catabolic enzymes, which may be favorable for the treatment of osteoarthritis [84]. In a related work, CS not only reduced the production of ROS, but also inhibited the secretion of inflammatory cytokines, such as IL-1 β and TNF- α [85]. Besides, CS has been shown to stimulate the production of proteoglycans by inhibiting the synthesis of proteolytic enzymes to lower apoptosis and cartilage matrix degeneration [86]. The expression levels of inflammatory cytokines were significantly lower in 3DCSS scaffold compared to 2DS and 3DS groups as assessed by RT-qPCR and Western blotting, which is in agreement with the DPPH assay. Moreover, the anti-inflammatory effect of 3DCSS over CS-free groups may attenuate inflammation and promote cartilaginous tissue regeneration.

5. Conclusion

In summary, we designed novel 3D CS-crosslinked biomimetic porous nanofibrous scaffolds with precise thickness *via* gas foaming in a pre-designed mold and subsequent freeze-drying for promoting cartilage regeneration and moderating joint inflammation. 3D gas-foamed scaffolds demonstrated low density, appropriate porosity and fast water absorption. Moreover, they preserved nano-topographical architecture with multilayered structures and stable mechanical properties. All of the scaffolds exhibited good cytocompatibility, while 3D gas-foamed scaffolds promoted seeding efficiency and proliferation of chondrocytes than that of 2DS. More importantly, biomimetic 3DCSS displayed good biological outcomes than those of the other groups as evidenced by the formation of cartilage-specific ECM, significant regeneration of articular cartilage in a rabbit model and less expression of pro-inflammatory factors both *in vitro* and *in vivo*. Moreover, the better mechanical and biological properties of 3DCSS were effective for the regeneration of the articular cartilage. Taken together, this strategy of designing biomimetic scaffolds as well as improving their performance by gas foaming may have broad implications for CTE applications.

CRedit authorship contribution statement

YC: Investigation, Methodology, Formal analysis, Writing-original draft; WX: Investigation, Conceptualization, Data Curation; MS: Conceptualization, Review & Editing; DS: Conceptualization, Data Curation; XX: Investigation, Conceptualization; ZY: Conceptualization, Data Curation; ME: Investigation, Conceptualization; HE: Investigation, Conceptualization; YM: Investigation, Conceptualization; YL: Conceptualization, Funding acquisition, Review & editing; XM: Supervision, Funding acquisition, Review & editing. YC and WX contributed equally to this work. All authors read and approved the final manuscript.

Availability of data and materials

The datasets used and analyzed during the current study are available from the corresponding author on reasonable request.

Declaration of competing interest

The authors declare that they have no known competing financial interests or personal relationships that could have appeared to influence the work reported in this paper.

Acknowledgement

This research was supported by the Fundamental Research Funds for the Central Universities (2232019A3-07), National Natural Science Foundation of China (Nos. 81970091, 32050410286, 31771023, 3201101259), Science and Technology Commission of Shanghai Municipality (Nos. 19441902600, 20S31900900, 20DZ2254900), Program of Shanghai Academic/Technology Research Leader (19XD1431100), and Sino German Science Foundation Research Exchange Center (M-0263). National Advanced Functional Fiber Innovation Center (2021-fx020301), International Cooperation of 2021–2022 China and Poland Science and Technology Personnel Exchange Program (No. 17). This project was also supported by Researchers Supporting Project Number (RSP-2021/65), King Saud University, Riyadh, Saudi Arabia.

Appendix A. Supplementary data

Supplementary data to this article can be found online at <https://doi.org/10.1016/j.msec.2022.112643>.

References

- R.J. Lories, F.P. Luyten, The bone-cartilage unit in osteoarthritis, *Nat. Rev. Rheumatol.* 7 (2011) 43–49, <https://doi.org/10.1038/nrrheum.2010.197>.
- V.C. Mow, A. Ratcliffe, A. Robin Poole, Cartilage and diarthrodial joints as paradigms for hierarchical materials and structures, *Biomaterials* 13 (1992) 67–97, [https://doi.org/10.1016/0142-9612\(92\)90001-5](https://doi.org/10.1016/0142-9612(92)90001-5).
- E.A. Makris, A.H. Gomoll, K.N. Malizos, J.C. Hu, K.A. Athanasiou, Repair and tissue engineering techniques for articular cartilage, *Nat. Rev. Rheumatol.* 11 (2015) 21–34, <https://doi.org/10.1038/nrrheum.2014.157>.
- C.J. Moran, C. Pascual-Garrido, S. Chubinskaya, H.G. Potter, R.F. Warren, B.J. Cole, S.A. Rodeo, Restoration of articular cartilage, *J. Bone Jt. Surg. - Ser. A* 96 (2014) 336–344, <https://doi.org/10.2106/JBJS.L.01329>.
- S.T. Johnna, G.M. Antonios, Review: tissue engineering for regeneration of articular cartilage, *Biomaterials* 21 (2000) 431–440.
- S.P. Nukavarapu, D.L. Dorcenus, Osteochondral tissue engineering: current strategies and challenges, *Biotechnol. Adv.* 31 (2013) 706–721, <https://doi.org/10.1016/j.biotechadv.2012.11.004>.
- D. Nestic, R. Whiteside, M. Brittberg, D. Wendt, I. Martin, P. Mainil-Varlet, Cartilage tissue engineering for degenerative joint disease, *Adv. Drug Deliv. Rev.* 58 (2006) 300–322, <https://doi.org/10.1016/j.addr.2006.01.012>.
- D.J. Huey, J.C. Hu, K.A. Athanasiou, Unlike bone, cartilage regeneration remains elusive, *Science* (80-) 6933 (2012) 917–921.
- Y. Chen, M. Sha, M. Liu, Y. Morsi, X. Mo, Advanced fabrication for electrospun three-dimensional nanofiber aerogels and scaffolds, *Bioact. Mater.* 5 (2020) 963–979, <https://doi.org/10.1016/j.bioactmat.2020.06.023>.
- F. Zhou, X. Zhang, D. Cai, J. Li, Q. Mu, W. Zhang, S. Zhu, Y. Jiang, W. Shen, S. Zhang, H.W. Ouyang, Silk fibroin-chondroitin sulfate scaffold with immuno-inhibition property for articular cartilage repair, *Acta Biomater.* 63 (2017) 64–75, <https://doi.org/10.1016/j.actbio.2017.09.005>.
- W. Shen, X. Chen, Y. Hu, Z. Yin, T. Zhu, J. Hu, J. Chen, Z. Zheng, W. Zhang, J. Ran, B.C. Heng, J. Ji, W. Chen, H.W. Ouyang, Long-term effects of knitted silk-collagen sponge scaffold on anterior cruciate ligament reconstruction and osteoarthritis prevention, *Biomaterials* 35 (2014) 8154–8163, <https://doi.org/10.1016/j.biomaterials.2014.06.019>.
- B.A. Blakeney, A. Tambralli, J.M. Anderson, A. Andukuri, D.J. Lim, D.R. Dean, H.W. Jun, Cell infiltration and growth in a low density, uncompressed three-dimensional electrospun nanofibrous scaffold, *Biomaterials* 32 (2011) 1583–1590, <https://doi.org/10.1016/j.biomaterials.2010.10.056>.
- D. Jin, J. Hu, D. Xia, A. Liu, H. Kuang, J. Du, X. Mo, M. Yin, Evaluation of a simple off-the-shelf bi-layered vascular scaffold based on poly(L-lactide-co-ε-caprolactone)/silk fibroin in vitro and in vivo, *Int. J. Nanomedicine* 14 (2019) 4261–4276, <https://doi.org/10.2147/IJN.S205569>.
- T. Wu, J. Zhang, Y. Wang, B. Sun, X. Guo, Y. Morsi, H. El-Hamshary, M. El-Newehy, X. Mo, Development of dynamic liquid and conjugated electrospun poly(L-lactide-co-caprolactone)/collagen nanofibers for regulating vascular smooth muscle cells growth, *J. Biomed. Nanotechnol.* 13 (2017) 303–312, <https://doi.org/10.1166/jbn.2017.2352>.
- S.K. Boda, S. Chen, K. Chu, H.J. Kim, J. Xie, Electrospinning electrospun nanofiber segments into injectable microspheres for potential cell delivery, *ACS Appl. Mater. Interfaces* 10 (2018) 25069–25079, <https://doi.org/10.1021/acsami.8b06386>.
- S. Chen, J.V. John, A. McCarthy, M.A. Carlson, X. Li, J. Xie, Fast transformation of 2D nanofiber membranes into pre-molded 3D scaffolds with biomimetic and oriented porous structure for biomedical applications, *Appl. Phys. Rev.* 7 (2020), <https://doi.org/10.1063/1.5144808>.
- J. Jiang, M.A. Carlson, M.J. Teusink, H. Wang, M.R. MacEwan, J. Xie, Expanding two-dimensional electrospun nanofiber membranes in the third dimension by a modified gas-foaming technique, *ACS Biomater. Sci. Eng.* 1 (2015) 991–1001, <https://doi.org/10.1021/acsbomaterials.5b00238>.
- J. Jiang, S. Chen, H. Wang, M.A. Carlson, A.F. Gombart, J. Xie, CO₂-expanded nanofiber scaffolds maintain activity of encapsulated bioactive materials and promote cellular infiltration and positive host response, *Acta Biomater.* 68 (2018) 237–248, <https://doi.org/10.1016/j.actbio.2017.12.018>.
- M.K. Joshi, H.R. Pant, A.P. Tiwari, H.J. Kim, C.H. Park, C.S. Kim, Multi-layered macroporous three-dimensional nanofibrous scaffold via a novel gas foaming technique, *Chem. Eng. J.* 275 (2015) 79–88, <https://doi.org/10.1016/j.cej.2015.03.121>.
- X. Jing, H. Li, H.Y. Mi, Y.J. Liu, Y.M. Tan, Fabrication of fluffy shish-kebab structured nanofibers by electrospinning, CO₂ escaping foaming and controlled crystallization for biomimetic tissue engineering scaffolds, *Chem. Eng. J.* 372 (2019) 785–795, <https://doi.org/10.1016/j.cej.2019.04.194>.
- S. Chen, M.A. Carlson, Y.S. Zhang, Y. Hu, J. Xie, Fabrication of injectable and superelastic nanofiber rectangle matrices (“peanuts”) and their potential applications in hemostasis, *Biomaterials* 179 (2018) 46–59, <https://doi.org/10.1016/j.biomaterials.2018.06.031>.
- J. Jiang, Z. Li, H. Wang, Y. Wang, M.A. Carlson, M.J. Teusink, M.R. MacEwan, L. Gu, J. Xie, Expanded 3D nanofiber scaffolds: cell penetration, neovascularization, and host response, *Adv. Healthc. Mater.* 5 (2016) 2993–3003, <https://doi.org/10.1002/adhm.201600808>.
- K. Zhang, X. Bai, Z. Yuan, X. Cao, X. Jiao, Y. Li, Y. Qin, Y. Wen, X. Zhang, Layered nanofiber sponge with an improved capacity for promoting blood coagulation and wound healing, *Biomaterials* 204 (2019) 70–79, <https://doi.org/10.1016/j.biomaterials.2019.03.008>.
- F. Rao, Z. Yuan, M. Li, F. Yu, X. Fang, B. Jiang, Y. Wen, P. Zhang, Expanded 3D nanofiber sponge scaffolds by gas-foaming technique enhance peripheral nerve regeneration, *Artif. Cells, Nanomedicine, Biotechnol.* 47 (2019) 491–500, <https://doi.org/10.1080/21691401.2018.1557669>.
- W. Wei, Y. Ma, X. Yao, W. Zhou, X. Wang, C. Li, J. Lin, Q. He, S. Leptihn, H. Ouyang, Advanced hydrogels for the repair of cartilage defects and regeneration, *Bioact. Mater.* 6 (2021) 998–1011, <https://doi.org/10.1016/j.bioactmat.2020.09.030>.
- C. Foss, E. Merzari, C. Migliaresi, A. Motta, Silk fibroin/hyaluronic acid 3D matrices for cartilage tissue engineering, *Biomacromolecules* 14 (2013) 38–47, <https://doi.org/10.1021/bm301174x>.
- S. Varghese, N.S. Hwang, A.C. Canver, P. Theprungsirikul, D.W. Lin, J. Elisseeff, Chondroitin sulfate based niches for chondrogenic differentiation of mesenchymal stem cells, *Matrix Biol.* 27 (2008) 12–21, <https://doi.org/10.1016/j.matbio.2007.07.002>.
- H. Kuang, Y. Wang, Y. Shi, W. Yao, X. He, X. Liu, X. Mo, S. Lu, P. Zhang, Biomaterials construction and performance evaluation of hep / silk-PLCL composite nanofiber small-caliber artificial blood vessel graft, *Biomaterials* 259 (2020), <https://doi.org/10.1016/j.biomaterials.2020.120288>.
- B. Cao, J. Yin, S. Yan, L. Cui, X. Chen, Y. Xie, Porous scaffolds based on cross-linking of Poly(L-glutamic acid), *Macromol. Biosci.* 11 (2011) 427–434, <https://doi.org/10.1002/mabi.201000389>.
- W. Chen, S. Chen, Y. Morsi, H. El-Hamshary, M. El-Newehy, C. Fan, X. Mo, Supersubstrate 3D scaffold based on electrospun nanofibers for cartilage tissue engineering, *ACS Appl. Mater. Interfaces* 8 (2016) 24415–24425, <https://doi.org/10.1021/acsami.6b06825>.
- Y. Xu, D. Li, Z. Yin, A. He, M. Lin, G. Jiang, X. Song, X. Hu, Y. Liu, J. Wang, X. Wang, L. Duan, G. Zhou, Tissue-engineered trachea regeneration using decellularized trachea matrix treated with laser micropore technique, *Acta Biomater.* 58 (2017) 113–121, <https://doi.org/10.1016/j.actbio.2017.05.010>.
- G. Zhou, H. Jiang, Z. Yin, Y. Liu, Q. Zhang, C. Zhang, B. Pan, J. Zhou, X. Zhou, H. Sun, D. Li, A. He, Z. Zhang, W. Zhang, W. Liu, Y. Cao, In vitro regeneration of patient-specific ear-shaped cartilage and its first clinical application for auricular reconstruction, *EBioMedicine* 28 (2018) 287–302, <https://doi.org/10.1016/j.ebiom.2018.01.011>.
- Y. Xu, L. Duan, Y. Li, Y. She, J. Zhu, G. Zhou, G. Jiang, Y. Yang, Nanofibrillar decellularized Wharton’s jelly matrix for segmental tracheal repair, *Adv. Funct. Mater.* 30 (2020), <https://doi.org/10.1002/adfm.201910067>.
- M. Shafiq, Y. Zhang, D. Zhu, Z. Zhao, D.H. Kim, S.H. Kim, D. Kong, In situ cardiac regeneration by using neuropeptide substance P and IGF-1C peptide eluting heart patches, *Regen. Biomater.* 5 (2018) 303–316, <https://doi.org/10.1093/rb/rby021>.
- Y. Xu, Y. Xu, B. Bi, M. Hou, L. Yao, Q. Du, A. He, Y. Liu, C. Miao, X. Liang, X. Jiang, G. Zhou, Y. Cao, A moldable thermosensitive hydroxypropyl chitin hydrogel for 3D cartilage regeneration in vitro and in vivo, *Acta Biomater.* 108 (2020) 87–96, <https://doi.org/10.1016/j.actbio.2020.03.039>.
- Y. Chen, W. Xu, M. Shafiq, J. Tang, J. Hao, X. Xie, Z. Yuan, X. Xiao, Y. Liu, X. Mo, Three-dimensional porous gas-foamed electrospun nanofiber scaffold for cartilage regeneration, *J. Colloid Interface Sci.* 603 (2021) 94–109, <https://doi.org/10.1016/j.jcis.2021.06.067>.
- D. Yan, G. Zhou, X. Zhou, W. Liu, W.J. Zhang, X. Luo, L. Zhang, T. Jiang, L. Cui, Y. Cao, The impact of low levels of collagen IX and pyridinoline on the mechanical properties of in vitro engineered cartilage, *Biomaterials* 30 (2009) 814–821, <https://doi.org/10.1016/j.biomaterials.2008.10.042>.
- G. Kesava Reddy, C.S. Enwemeka, A simplified method for the analysis of hydroxyproline in biological tissues, *Clin. Biochem.* 29 (1996) 225–229, [https://doi.org/10.1016/0009-9120\(96\)00003-6](https://doi.org/10.1016/0009-9120(96)00003-6).
- M. Shafiq, Y. Jung, S.H. Kim, In situ vascular regeneration using substance P-immobilised poly(L-lactide-co-ε-caprolactone) scaffolds: stem cell recruitment, angiogenesis, and tissue regeneration, *Eur. Cells Mater.* 30 (2015) 282–302, <https://doi.org/10.22203/eCM.v030a20>.

- [40] Z. Zou, M. Wei, J. Fang, W. Dai, T. Sun, Q. Liu, G. Gong, Y. Liu, S. Song, F. Ma, L. Wang, L. Huang, Z. Wang, Preparation of chondroitin sulfates with different molecular weights from bovine nasal cartilage and their antioxidant activities, *Int. J. Biol. Macromol.* 152 (2020) 1047–1055, <https://doi.org/10.1016/j.ijbiomac.2019.10.192>.
- [41] J. Almodóvar, L.W. Place, J. Gogolski, K. Erickson, M.J. Kipper, Layer-by-layer assembly of polysaccharide-based polyelectrolyte multilayers: a spectroscopic study of hydrophilicity, composition, and ion pairing, *Biomacromolecules* 12 (2011) 2755–2765, <https://doi.org/10.1021/bm200519y>.
- [42] W. Yu, R. Wanka, J.A. Finlay, J.L. Clarke, A.S. Clare, A. Rosenhahn, Degradable hyaluronic acid/chitosan polyelectrolyte multilayers with marine fouling-release properties, *Biofouling* (2020) 1–22, <https://doi.org/10.1080/08927014.2020.1846725>.
- [43] R.N. Oosterbeek, K.A. Kwon, P. Duffy, S. McMahon, X.C. Zhang, S.M. Best, R.E. Cameron, Tuning structural relaxations, mechanical properties, and degradation time-scale of PLLA during hydrolytic degradation by blending with PLCL-PEG, *Polym. Degrad. Stab.* 170 (2019), 109015, <https://doi.org/10.1016/j.polymdegradstab.2019.109015>.
- [44] J. Xue, T. Wu, Y. Dai, Y. Xia, Electrospinning and electrospun nanofibers: methods, materials, and applications, *Chem. Rev.* 119 (2019) 5298–5415, <https://doi.org/10.1021/acs.chemrev.8b00593>.
- [45] W. Chen, Y. Xu, Y. Liu, Z. Wang, Y. Li, G. Jiang, X. Mo, G. Zhou, Three-dimensional printed electrospun fiber-based scaffold for cartilage regeneration, *Mater. Des.* 179 (2019), 107886, <https://doi.org/10.1016/j.matdes.2019.107886>.
- [46] Y. Si, J. Yu, X. Tang, J. Ge, B. Ding, Ultralight nanofiber-assembled cellular aerogels with superelasticity and multifunctionality, *Nat. Commun.* 5 (2014) 5802, <https://doi.org/10.1038/ncomms6802>.
- [47] J. Song, G. Zhu, H. Gao, L. Wang, N. Li, X. Shi, Y. Wang, Origami meets electrospinning: a new strategy for 3D nanofiber scaffolds, *Bio-Design Manuf.* 1 (2018) 254–264, <https://doi.org/10.1007/s42242-018-0027-9>.
- [48] W. Chen, Y. Xu, Y. Li, L. Jia, X. Mo, G. Jiang, G. Zhou, 3D printing electrospinning fiber-reinforced decellularized extracellular matrix for cartilage regeneration, *Chem. Eng. J.* (2019), 122986, <https://doi.org/10.1016/j.cej.2019.122986>.
- [49] S. Chen, H. Wang, A. McCarthy, Z. Yan, H.J. Kim, M.A. Carlson, Y. Xia, J. Xie, Three-dimensional objects consisting of hierarchically assembled nanofibers with controlled alignments for regenerative medicine, *Nano Lett.* 19 (2019) 2059–2065, <https://doi.org/10.1021/acs.nanolett.9b00217>.
- [50] Y. Chen, Z. Jia, M. Shafiq, X. Xie, X. Xiao, R. Castro, J. Rodrigues, J. Wu, G. Zhou, X. Mo, Gas foaming of electrospun poly(L-lactide-co-caprolactone)/silk fibroin nanofiber scaffolds to promote cellular infiltration and tissue regeneration, *Colloids Surf. B: Biointerfaces* 201 (2021), 111637, <https://doi.org/10.1016/j.colsurfb.2021.111637>.
- [51] C.H.U. Kum, Y. Cho, S.H.O. Seo, Y.K.I. Joung, D.J. Un. Ahn, D.K.Eu. Han, A poly(lactide) stereocomplex structure with modified magnesium oxide and its effects in enhancing the mechanical properties and suppressing inflammation, *Small* 10 (2014) 3783–3794, <https://doi.org/10.1002/sml.201302880>.
- [52] A. Pangesty, M. Todo, Preparation and characterization of porous tubular scaffold made of PCL/PLCL blends for vascular tissue engineering, *J. Mech. Eng. Sci.* 4 (2017) 184–196.
- [53] M. Abedalwafa, F. Wang, L. Wang, C. Li, Biodegradable poly-epsilon-caprolactone (PCL) for tissue engineering applications: a review, *Rev. Adv. Mater. Sci.* 34 (2013) 123–140.
- [54] H. Kuang, Y. Wang, J. Hu, C. Wang, S. Lu, X. Mo, A method for preparation of an internal layer of artificial vascular graft co-modified with salivianic acid B and heparin, *ACS Appl. Mater. Interfaces* 10 (2018) 19365–19372, <https://doi.org/10.1021/acsami.8b02602>.
- [55] X. Xie, J. Cai, Y. Yao, Y. Chen, A.ur R. Khan, J. Wu, X. Mo, A woven scaffold with continuous mineral gradients for tendon-to-bone tissue engineering, *Compos. Part B* 212 (2021), 108679, <https://doi.org/10.1016/j.compositesb.2021.108679>.
- [56] B. Sun, Z. Zhou, T. Wu, W. Chen, D. Li, H. Zheng, H. El-Hamshary, S.S. Al-Deyab, X. Mo, Y. Yu, Development of nanofiber sponges-containing nerve guidance conduit for peripheral nerve regeneration in vivo, *ACS Appl. Mater. Interfaces* 9 (2017) 26684–26696, <https://doi.org/10.1021/acsami.7b06707>.
- [57] Z. Wang, M. Lin, Q. Xie, H. Sun, Y. Huang, D.D. Zhang, Z. Yu, X. Bi, J. Chen, J. Wang, W. Shi, P. Gu, X. Fan, Electrospun silk fibroin/poly(lactide-co-epsilon-caprolactone) nanofibrous scaffolds for bone regeneration, *Int. J. Nanomedicine* 11 (2016) 1483–1500, <https://doi.org/10.2147/IJN.S97445>.
- [58] Y. Jung, M.S. Park, J.W. Lee, Y.H. Kim, S.H. Kim, S.H. Kim, Cartilage regeneration with highly-elastic three-dimensional scaffolds prepared from biodegradable poly(l-lactide-co-epsilon-caprolactone), *Biomaterials* 29 (2008) 4630–4636, <https://doi.org/10.1016/j.biomaterials.2008.08.031>.
- [59] Y.J. Lin, C.J. Liao, C.F. Chen, W. Tsai, Porous biodegradable polymer scaffolds for cartilage tissue engineering, *Third Smith Nephew Int. Symp. - Transl. Tissue Eng. into Prod* 2002, p. 122.
- [60] S. Çalamak, C. Erdoğan, M. Özalp, K. Ulubayram, Silk fibroin based antibacterial bionanotextiles as wound dressing materials, *Mater. Sci. Eng. C* 43 (2014) 11–20, <https://doi.org/10.1016/j.msec.2014.07.001>.
- [61] M. Shafiq, D. Kong, S.H. Kim, SDF-1 α peptide tethered polyester facilitates tissue repair by endogenous cell mobilization and recruitment, *J. Biomed. Mater. Res. A* 105 (2017) 2670–2684, <https://doi.org/10.1002/jbm.a.36130>.
- [62] X. Xie, Y. Chen, X. Wang, X. Xu, Y. Shen, A.ur R. Khan, A. Aldabahi, A.E. Fetz, G.L. Bowlin, M. El-Newehy, X. Mo, Electrospinning nanofiber scaffolds for soft and hard tissue regeneration, *J. Mater. Sci. Technol.* 59 (2020) 243–261, <https://doi.org/10.1016/j.jmst.2020.04.037>.
- [63] W. Fan, J. Li, L. Yuan, J. Chen, Z. Wang, Y. Wang, C. Guo, X. Mo, Z. Yan, Intra-articular injection of kartogenin-conjugated polyurethane nanoparticles attenuates the progression of osteoarthritis, *Drug Deliv.* 25 (2018) 1004–1012, <https://doi.org/10.1080/10717544.2018.1461279>.
- [64] J.Y. Reginster, N. Veronese, Highly purified chondroitin sulfate: a literature review on clinical efficacy and pharmacoeconomic aspects in osteoarthritis treatment, *Aging Clin. Exp. Res.* (2020), <https://doi.org/10.1007/s40520-020-01643-8>.
- [65] M. Iovu, G. Dumais, P. du Souich, Anti-inflammatory activity of chondroitin sulfate, *Osteoarthr. Cartil.* 16 (2008) 14–18, <https://doi.org/10.1016/j.joca.2008.06.008>.
- [66] D. Uebelhart, Clinical review of chondroitin sulfate in osteoarthritis, *Osteoarthr. Cartil.* 16 (2008) 19–21, <https://doi.org/10.1016/j.joca.2008.06.006>.
- [67] Q. Shen, C. Zhang, H. Mo, H. Zhang, X. Qin, J. Li, Z. Zhang, A. Richel, Fabrication of chondroitin sulfate calcium complex and its chondrocyte proliferation in vitro, *Carbohydr. Polym.* 254 (2021), 117282, <https://doi.org/10.1016/j.carbpol.2020.117282>.
- [68] T. A. V. S. Mohanty, A.K. Dinda, V. Koul, Fabrication and evaluation of gelatin/hyaluronic acid/chondroitin sulfate/asiatic acid based biopolymeric scaffold for the treatment of second-degree burn wounds - Wistar rat model study, *Biomed. Mater.* 15 (2020), <https://doi.org/10.1088/1748-605X/ab8721>.
- [69] S. Bhowmick, S. Rother, H. Zimmermann, P.S. Lee, S. Moeller, M. Schnabelrauch, V. Koul, R. Jordan, V. Hintze, D. Scharnweber, Biomimetic electrospun scaffolds from main extracellular matrix components for skin tissue engineering application - the role of chondroitin sulfate and sulfated hyaluronan, *Mater. Sci. Eng. C* 79 (2017) 15–22, <https://doi.org/10.1016/j.msec.2017.05.005>.
- [70] M. Pezeshki-Modaress, H. Mirzadeh, M. Zandi, S. Rajabi-Zeleti, N. Sodeifi, N. Aghdami, M.R.K. Mofrad, Gelatin/chondroitin sulfate nanofibrous scaffolds for stimulation of wound healing: in-vitro and in-vivo study, *J. Biomed. Mater. Res. - Part A* 105 (2017) 2020–2034, <https://doi.org/10.1002/jbm.a.35890>.
- [71] A. Sadeghi, M. Pezeshki-Modaress, M. Zandi, Electrospun polyvinyl alcohol/gelatin/chondroitin sulfate nanofibrous scaffold: fabrication and in vitro evaluation, *Int. J. Biol. Macromol.* 114 (2018) 1248–1256, <https://doi.org/10.1016/j.ijbiomac.2018.04.002>.
- [72] S. Yan, Q. Zhang, J. Wang, Y. Liu, S. Lu, M. Li, D.L. Kaplan, Silk fibroin/chondroitin sulfate/hyaluronic acid ternary scaffolds for dermal tissue reconstruction, *Acta Biomater.* 9 (2013) 6771–6782, <https://doi.org/10.1016/j.actbio.2013.02.016>.
- [73] M. Naeimi, M. Fathi, M. Rafienia, S. Bonakdar, Silk fibroin-chondroitin sulfate-alginate porous scaffolds: structural properties and in vitro studies, *J. Appl. Polym. Sci.* 131 (2014) 1–9, <https://doi.org/10.1002/app.41048>.
- [74] Y. Yu, Y. Wang, C. Lu, D. Long, Q. Zhang, S. Yan, R. You, M. Li, Chondrogenic differentiation of rat mesenchymal stem cells on silk fibroin/chondroitin sulfate/hyaluronic acid ternary scaffolds, *Fibers Polym.* 17 (2016) 324–332, <https://doi.org/10.1007/s12221-016-5795-2>.
- [75] N. Sawatjui, T. Damrongrungruang, W. Leeansaksiri, P. Jearanaikoon, T. Limpiboon, Fabrication and characterization of silk fibroin-gelatin/chondroitin sulfate/hyaluronic acid scaffold for biomedical applications, *Mater. Lett.* 126 (2014) 207–210, <https://doi.org/10.1016/j.matlet.2014.04.018>.
- [76] Q. Gao, H. Gu, P. Zhao, C. Zhang, M. Cao, J. Fu, Y. He, Fabrication of electrospun nanofibrous scaffolds with 3D controllable geometric shapes, *Mater. Des.* 157 (2018) 159–169, <https://doi.org/10.1016/j.matdes.2018.07.042>.
- [77] S. Chen, A. McCarthy, J.V. John, Y. Su, J. Xie, Converting 2D nanofiber membranes to 3D hierarchical assemblies with structural and compositional gradients regulates cell behavior, *Adv. Mater.* 32 (2020) 1–10, <https://doi.org/10.1002/adma.202003754>.
- [78] B. Sun, J. Li, W. Liu, B.M. Aqeel, H. El-Hamshary, S.S. Al-Deyab, X. Mo, Fabrication and characterization of mineralized P(LLA-CL)/SF three-dimensional nanofiber scaffolds, *Iran, Polym. J.* 24 (2014) 29–40, <https://doi.org/10.1007/s13726-014-0297-9> (English Ed).
- [79] W. Chen, Y. Xu, Y. Liu, Z. Wang, Y. Li, G. Jiang, X. Mo, G. Zhou, Three-dimensional printed electrospun fiber-based scaffold for cartilage regeneration, *Mater. Des.* (2019), 107886, <https://doi.org/10.1016/j.matdes.2019.107886>.
- [80] W.C. Puelacher, S.W. Kim, J.P. Vacanti, B. Schloo, D. Mooney, C.A. Vacanti, Tissue-engineered growth of cartilage: the effect of varying the concentration of chondrocytes seeded onto synthetic polymer matrices, *Int. J. Oral Maxillofac. Surg.* 23 (1994) 49–53, [https://doi.org/10.1016/S0901-5027\(05\)80328-5](https://doi.org/10.1016/S0901-5027(05)80328-5).
- [81] V.F. Sechrist, Y.J. Miao, C. Niyibizi, A. Westerhausen-Larson, H.W. Matthew, C.H. Evans, F.H. Fu, J.K. Suh, GAG-augmented polysaccharide hydrogel: a novel biocompatible and biodegradable material to support chondrogenesis, *J. Biomed. Mater. Res.* 49 (2000) 534–541, [https://doi.org/10.1002/\(sici\)1097-4636\(20000315\)49:4<534::aid-jbm12>3.0.co;2-%23](https://doi.org/10.1002/(sici)1097-4636(20000315)49:4<534::aid-jbm12>3.0.co;2-%23).
- [82] F. Legendre, C. Bauge, R. Roche, A.S. Saurel, J.P. Pujol, Chondroitin sulfate modulation of matrix and inflammatory gene expression in IL-1 β -stimulated chondrocytes - study in hypoxic alginate bead cultures, *Osteoarthr. Cartil.* 16 (2008) 105–114, <https://doi.org/10.1016/j.joca.2007.05.020>.
- [83] J.A. Hubbell, Materials as morphogenetic guides in tissue engineering, *Curr. Opin. Biotechnol.* 14 (2003) 551–558, <https://doi.org/10.1016/j.copbio.2003.09.004>.
- [84] S. Abe, Y. Obata, S. Oka, T. Koji, T. Nishino, K. Izumikawa, Chondroitin sulfate prevents peritoneal fibrosis in mice by suppressing NF- κ B activation, *Med. Mol. Morphol.* 49 (2016) 144–153, <https://doi.org/10.1007/s00795-016-0133-8>.
- [85] M. Woo, D.H. Kwon, Y.H. Choi, J.S. Noh, Inhibitory effects of skate cartilage chondroitin sulfate-rich extract on the production of inflammatory mediators and ROS in lipopolysaccharide-treated murine macrophages: a comparison with shark cartilage chondroitin sulfate, *In Vitro Cell. Dev. Biol. Anim.* 56 (2020) 271–276, <https://doi.org/10.1007/s11626-020-00443-8>.
- [86] R.A.A. Muzzarelli, F. Greco, A. Busilacchi, V. Sollazzo, A. Gigante, Chitosan, hyaluronan and chondroitin sulfate in tissue engineering for cartilage regeneration: a review, *Carbohydr. Polym.* 89 (2012) 723–739, <https://doi.org/10.1016/j.carbpol.2012.04.057>.